J. Fluid Mech. (2012), *vol.* 707, *pp.* 74–110.
doi:10.1017/jfm.2012.265

Evolution of enstrophy in shock/homogeneous turbulence interaction

Krishnendu Sinha†

Department of Aerospace Engineering, Indian Institute of Technology Bombay, Mumbai 400076, India

(Received 19 April 2011; revised 21 January 2012; accepted 4 June 2012;
first published online 8 August 2012)

Interaction of turbulent fluctuations with a shock wave plays an important role in many high-speed flow applications. This paper studies the amplification of enstrophy, defined as mean-square fluctuating vorticity, in homogeneous isotropic turbulence passing through a normal shock. Linearized Navier–Stokes equations written in a frame of reference attached to the unsteady shock wave are used to derive transport equations for the vorticity components. These are combined to obtain an equation that describes the evolution of enstrophy across a time-averaged shock wave. A budget of the enstrophy equation computed using results from linear interaction analysis and data from direct numerical simulations identifies the dominant physical mechanisms in the flow. Production due to mean flow compression and baroclinic torques are found to be the major contributors to the enstrophy amplification. Closure approximations are proposed for the unclosed correlations in the production and baroclinic source terms. The resulting model equation is integrated to obtain the enstrophy jump across a shock for a range of upstream Mach numbers. The model predictions are compared with linear theory results for varying levels of vortical and entropic fluctuations in the upstream flow. The enstrophy model is then cast in the form of k–ϵ equations and used to compute the interaction of homogeneous isotropic turbulence with normal shocks. The results are compared with available data from direct numerical simulations. The equations are further used to propose a model for the amplification of turbulent viscosity across a shock, which is then applied to a canonical shock–boundary layer interaction. It is shown that the current model is a significant improvement over existing models, both for homogeneous isotropic turbulence and in the case of complex high-speed flows with shock waves.

Key words: compressible turbulence, high-speed flow, turbulence modelling

1. Introduction

Turbulent flows are marked by a high level of fluctuating vorticity, and these vortical fluctuations play an important role in the dynamics of turbulent motion. Enstrophy, defined as the mean-square vorticity fluctuations, represents the intensity of rotation of turbulence and is a quantity of fundamental interest in a turbulent flow. It is mainly associated with the small-scale motion, and thus determines the resolution requirement of direct numerical simulation (DNS) of a turbulence field. The turbulent kinetic energy k is dissipated into heat by the action of viscous stresses. In homogeneous

† Email address for correspondence: krish@aero.iitb.ac.in

incompressible turbulence, the dissipation rate ϵ can be expressed as the product of enstrophy and the mean kinematic viscosity of the fluid. In compressible flows, enstrophy is related to the solenoidal dissipation rate ϵ_s, which is a dominant part of turbulent dissipation in wall-bounded shear flows. The quantities k, ϵ and enstrophy are often used to characterize the state of turbulence in the Reynolds-averaged Navier–Stokes (RANS) framework.

Interaction of turbulent fluctuations with shock waves is common in supersonic and hypersonic flow applications. In the case of aerospace vehicles, shock–boundary layer interactions are often present on deflected control surfaces, wing–body junctions, intakes of air-breathing engines and rocket nozzles. Impingement of the shock generated by the engine cowl, for example, can significantly alter the turbulent boundary layer on the inlet walls. Typical effects include flow separation and reattachment, localized high pressure rise and enhanced heat transfer, which are detrimental to the performance and operability of the engine. Accurate prediction of shock–boundary layer interaction (SBLI) flows poses a significant challenge to numerical simulations based on RANS methodology (Roy & Blottner 2006). Uncertainty in the predictions of current turbulence models often require large design margins for practical applications.

The amplification of boundary layer turbulence due to the shock lies at the core of SBLI flows. It directly influences the extent of flow separation, and therefore determines the topology of shocks and expansion waves generated by the separation bubble. See, for example, the simulation of an oblique shock impinging on a turbulent boundary layer by Pasha & Sinha (2008) and hypersonic cone–flare configurations by Pasha & Sinha (2012). Accurate prediction of the flow topology is essential to obtain the correct variation of surface properties. Wall skin friction coefficient and heat flux are also a strong function of the turbulence level in the near-wall region. Predicting the state of the downstream turbulence, specifically the post-shock levels of k, ϵ and enstrophy, is therefore important in these interactions.

Shock/turbulence interaction is a complex process involving several physical phenomena. Bulk compression at the shock amplifies the turbulent fluctuations. The turbulent length scales, like the Kolmogorov scale and Taylor microscale, decrease across the shock (Larsson & Lele 2009). Turbulent fluctuations in the incoming flow cause local distortion and unsteadiness of the shock wave. The unsteady shock motion is found to have a damping effect on the streamwise velocity fluctuations (Sinha, Mahesh & Candler 2003). The level of turbulence amplification also depends on the nature of upstream turbulence – namely, the relative magnitude of and correlation between the acoustic, entropic and vortical components (Kovasznay 1953). For example, turbulence amplification is significantly enhanced in the presence of negatively correlated temperature and velocity fluctuations in the incoming flow (Mahesh, Lele & Moin 1997). The interaction of turbulence with a shock wave is thus a complex interplay of different physical processes. Understanding these mechanisms at the shock and predicting the turbulence amplification accurately is therefore a challenging task.

Vorticity generation at a gas dynamic discontinuity has been the subject of several previous studies, see for example, Hayes (1957) and Berndt (1966). More recently, Kevlahan (1997) summarized the earlier results, and derived a general expression for the vorticity jump across a shock wave. He considered several scenarios of steady and unsteady shocks propagating into uniform and non-uniform flows, and reproduced the results presented by Hayes (1957). It is found that the vorticity production at the shock is caused by three physical mechanisms: shock focusing, baroclinic torques and

conservation of angular momentum at the shock wave. The role of non-uniformities in the upstream flow in generating vorticity at the shock is emphasized by Kevlahan (1997). In this regard, the interaction of turbulence with shock waves is of particular interest, and the contribution of the different mechanisms in vorticity generation when weak/strong turbulence passes through a weak/strong shock are discussed.

The objective of the current work is to study the evolution of vorticity components ω_i' for $i = 1$, 2 and 3, and the resulting amplification of enstrophy $\overline{\omega_i'\omega_i'}$ across a shock wave. The key physical processes are to be identified and modelled in a physically consistent way so as to predict the downstream level of $\overline{\omega_i'\omega_i'}$ accurately. The model problem chosen for the study is the interaction of homogeneous isotropic turbulence with a normal shock. It is a fundamental problem that isolates the effect of a shock wave on turbulent fluctuations. It eliminates other effects like flow separation, reattachment and streamline curvature that are commonly present in shock/turbulent boundary layer interactions. Availability of DNS data (Mahesh *et al.* 1997; Jamme *et al.* 2002; Larsson & Lele 2009) for homogeneous turbulence passing through a normal shock wave provides insight into the underlying physical processes. The dominant mechanisms can thus be identified for detailed analysis and modelling. In addition, turbulence amplification computed in the DNS can serve as a benchmark for comparing existing and new models.

Mahesh *et al.* (1997) apply linear interaction analysis (LIA) to study the interaction of homogeneous turbulence with a normal shock. The upstream turbulence field is represented as a combination of vorticity and entropy waves. In the linear inviscid framework, each wave interacts independently with the shock, which is treated as a discontinuity. Superposition of the resulting waves, for a given upstream energy spectrum, yields the turbulence field downstream of the shock. The analysis is based on the assumption that the turbulent fluctuations are small in magnitude compared to the variations in the mean flow quantities. Inter-modal interactions are expected to be negligible at the shock as long as $M_t^2 \ll M_1^2 - 1$ (Lee, Lele & Moin 1993). Here, M_t and M_1 are the turbulence and mean flow Mach numbers in the incoming flow.

The linear analysis is found to reproduce several key aspects of shock–turbulence interaction that are observed in DNS. For example, it predicts the non-monotonic behaviour of the streamwise Reynolds stress behind the shock due to a rapid decay of acoustic energy (Mahesh *et al.* 1997). It also matches the DNS amplification of turbulent kinetic energy across the shock wave (Sinha *et al.* 2003). On the other hand, the theory does not predict the amplification of individual Reynolds stresses correctly (Larsson & Lele 2009). It also does not reproduce the rapid increase in streamwise vorticity variance downstream of the shock wave. In spite of these limitations, LIA provides valuable insight into the underlying physical processes. Results from the analysis have therefore proved useful in developing advanced turbulence models for shock–turbulence interaction. Some of the work in this direction is summarized below.

Sinha *et al.* (2003) study the effect of unsteady shock motion on turbulence amplification across a shock. They start by deriving a transport equation for the turbulent kinetic energy in a frame of reference attached to the instantaneous shock wave. The shock-unsteadiness effect appears as a negative source term in the k-equation, and involves a correlation between the streamwise velocity fluctuations and the unsteady shock speed. The correlation is found to be positive, implying an in-phase coupling between the two quantities. Specifically, a positive streamwise velocity fluctuation results in a downstream motion of the shock wave, and vice-versa. The correlation coefficient is obtained from linear analysis results and a model is developed

for the damping effect of the unsteady shock motion. The resulting equation is found to yield an accurate prediction of the turbulent kinetic energy amplification across a normal shock, for purely vortical turbulence in the incoming flow.

In a subsequent work, Veera & Sinha (2009) study the effect of upstream temperature fluctuations on k-amplification in shock/homogeneous turbulence interaction. It is found that the primary effect of upstream temperature fluctuations is via the mean pressure-gradient production term. The source term has a vanishing contribution for purely vortical turbulence upstream of the shock, and its magnitude increases with the level of incoming temperature fluctuation. The production due to mean pressure gradient involves a correlation between the temperature and streamwise velocity fluctuations, such that it is positive for negatively correlated temperature and velocity fluctuations in the incoming turbulence. The source term is negative when the upstream temperature fluctuations are positively correlated with the streamwise velocity fluctuations. A model for the source term is developed using linear theory results, and it reproduces the physical effect correctly.

In this paper, an equation describing the evolution of enstrophy across a nominally normal shock is derived. The starting point is the Navier–Stokes equations written in a frame of reference attached to the unsteady shock wave. This coordinate transformation brings the shock unsteadiness and distortion effects into the governing equations. A separation of scales between the rapid changes across the shock and the relatively slower variation due to turbulence is assumed to identify the leading-order terms. The resulting equations are linearized about a steady one-dimensional mean flow, and are then used to derive a transport equation for the streamwise vorticity fluctuations. An equation for the transverse vorticity components is derived by considering the streamwise derivative of the linearized momentum equations. Here, it is important to separate the streamwise gradient caused by the shock wave from those due to turbulent fluctuations that contribute to the turbulent vorticity. The transport equations for the vorticity components, thus obtained, are combined to give an equation for the evolution of enstrophy across the shock wave.

Next, the Rankine–Hugoniot relations applied to the unsteady shock wave are linearized, and a procedure similar to that described above is followed to arrive at an integrated form of the enstrophy equation. Results from LIA of Mahesh *et al.* (1997) and DNS of Larsson & Lele (2009) are used to compute a budget of the enstrophy amplification as a function of the shock strength for different types of inflow turbulence. The relative magnitude of the source terms is evaluated to identify the dominant mechanisms that contribute to enstrophy amplification in each case. Models are then proposed for the unclosed correlations and the resulting equation is integrated analytically to obtain the amplification of enstrophy across the shock wave in the high-Reynolds-number limit. The accuracy of the model is evaluated against predictions of the linear theory (Mahesh *et al.* 1997).

Finally, the model predictions are compared with DNS of shock/homogeneous turbulence interaction and experimental results for a canonical SBLI flow. For this purpose, the modelled enstrophy equation is combined with an equation for the turbulence kinetic energy from earlier work (Veera & Sinha 2009), and cast in the form of a k–ϵ turbulence model. The equations are then numerically integrated along with the mean flow conservation equations, and the resulting evolution of turbulent kinetic energy and solenoidal dissipation rate are compared with the DNS data. Test cases corresponding to different types of inflow turbulence for varying upstream mean flow Mach number are considered. The effects of numerical error incurred at the shock wave are also discussed. For the SBLI test case, the k–ϵ model equations are

used to propose a model for the amplification of the turbulent viscosity at the shock. Simulations are performed in the framework of the Spalart–Allmaras (SA) turbulence model and the surface predictions are compared with experimental measurements.

It is assumed that the turbulence upstream of the shock is composed of vortical and entropic fluctuations. As per Morkovin's hypothesis, turbulent fluctuations in a compressible boundary layer are essentially composed of vorticity and entropy modes, i.e. the acoustic component is negligible. Fluctuations in total temperature are also assumed to be small, which results in the following relation between the thermodynamic and velocity fields:

$$\frac{\rho'}{\bar{\rho}} = -\frac{T'}{\overline{T}} = (\gamma - 1)M^2\frac{u'}{\bar{u}}, \tag{1.1}$$

where ρ, T and u are density, temperature and streamwise velocity, M is the mean flow Mach number, and γ is the ratio of specific heats at constant pressure and at constant volume. An overbar represents Reynolds averaging, while a prime indicates the fluctuating part.

The turbulence upstream of the shock is considered to be homogeneous and isotropic, with the thermodynamic field related to the velocity fluctuations by

$$\frac{\rho'}{\bar{\rho}} = -\frac{T'}{\overline{T}} = A_{uT}\frac{u'}{\bar{u}}. \tag{1.2}$$

Here, the acoustic fluctuations are neglected ($p' = 0$) and Morkovin's hypothesis is satisfied for $A_{uT} = (\gamma - 1)M^2$. The term A_{uT} can be interpreted as the ratio of normalized temperature and velocity fluctuations. Constant values of A_{uT} are chosen and the amplification of $\overline{\omega_i'\omega_i'}$ across a normal shock is studied for a given A_{uT} as a function of the upstream Mach number. $A_{uT} = 0$ corresponds to purely vortical turbulence upstream of the shock. Negatively correlated upstream velocity and temperature fluctuations are considered for $A_{uT} = 0.58$, 1, 2 and 4, where the magnitude of temperature and density fluctuations increase with increasing A_{uT}. A case with positive velocity–temperature correlation in the incoming flow ($A_{uT} = -0.58$) is also studied. Note that the cases $A_{uT} = 0.58$ and -0.58 are analysed by Mahesh *et al.* (1997).

2. Transport equation for enstrophy

A uniform mean flow is considered upstream and downstream of a normal shock, with x as the shock-normal direction. The shock wave is steady in the mean, and undergoes small deviations from its mean position in response to the turbulent fluctuations. The deviation of the shock is denoted by $\xi(y, z, t)$, such that the temporal derivative ξ_t denotes the streamwise velocity of the shock wave, and the transverse derivatives ξ_y and ξ_z represent the angular distortions of the shock in the x–y and x–z planes respectively (see figure 1).

A frame of reference stationary with respect to the shock wave is denoted by $x^{(1)}, x^{(2)}, x^{(3)}$. The instantaneous shock-normal direction is along $x^{(1)}$, and the axes $x^{(2)}$ and $x^{(3)}$ are in a plane parallel to the shock wave (see figure 1). For small shock distortions,

$$x^{(1)} = x - \xi - y\xi_y - z\xi_z, \tag{2.1a}$$

$$x^{(2)} = x\xi_y + y, \tag{2.1b}$$

$$x^{(3)} = x\xi_z + z, \tag{2.1c}$$

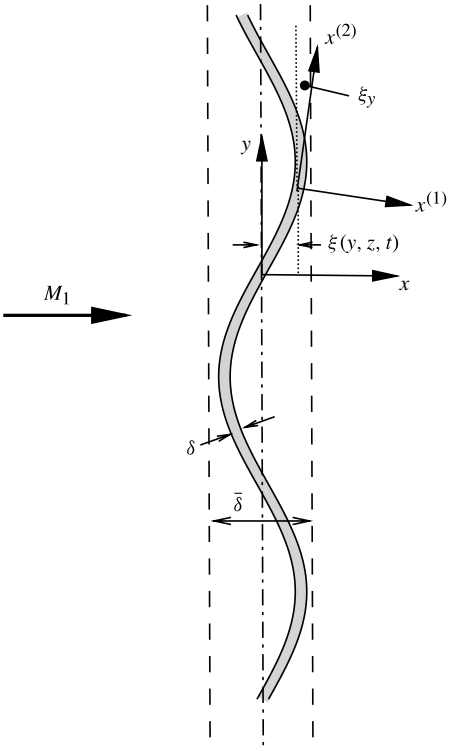

FIGURE 1. Schematic showing a distorted shock wave caused by the interaction with turbulent fluctuations.

where higher-order terms are neglected. The corresponding velocity components are given by

$$u^{(1)} = u - \xi_t - v\xi_y - w\xi_z \simeq \bar{u} + u' - \xi_t, \tag{2.2a}$$

$$u^{(2)} = u\xi_y + v \simeq \bar{u}\xi_y + v', \tag{2.2b}$$

$$u^{(3)} = u\xi_z + w \simeq \bar{u}\xi_z + w', \tag{2.2c}$$

where u, v, w are the velocity components in the (x, y, z) coordinate system. The transverse velocity components $\bar{v} = \bar{w} = 0$ in the one-dimensional mean flow, and higher-order terms are neglected, once again, owing to small distortions of the shock wave from its mean location. Also, the fluctuations are assumed to be small compared to the changes in the mean flow variables. In the following derivation, Reynolds averaging ($u = \bar{u} + u'$) is used instead of Favre averaging ($u = \tilde{u} + u''$). This is because $\bar{u} \simeq \tilde{u}$ and $u' \simeq u''$ in the linear limit.

We start with the momentum conservation equation in the shock-normal direction:

$$\frac{\partial \rho u^{(1)}}{\partial t} + \frac{\partial \rho u^{(1)}u^{(1)}}{\partial x^{(1)}} + \frac{\partial \rho u^{(1)}u^{(2)}}{\partial x^{(2)}} + \frac{\partial \rho u^{(1)}u^{(3)}}{\partial x^{(3)}} + \frac{\partial p}{\partial x^{(1)}} = \frac{\partial \sigma_{11}}{\partial x^{(1)}} + \frac{\partial \sigma_{12}}{\partial x^{(2)}} + \frac{\partial \sigma_{13}}{\partial x^{(3)}}, \tag{2.3}$$

where ρ and p are density and pressure respectively, and σ_{ij} is the viscous stress tensor. The equation is written in conservative form for the instantaneous variables for a finite-thickness shock wave. The shock-parallel variations along $x^{(2)}$ and $x^{(3)}$ are caused by the turbulent fluctuations, and the corresponding derivatives scale as the turbulent length scale ℓ. On the other hand, the derivatives in the shock-normal direction $x^{(1)}$ are due to the shock gradient, with the instantaneous shock thickness δ as the characteristic length scale. Noting that $\delta \ll \ell$, we have

$$\frac{\partial}{\partial x^{(1)}} \sim \frac{1}{\delta} \gg \frac{1}{\ell} \sim \frac{\partial}{\partial x^{(2)}} \sim \frac{\partial}{\partial x^{(3)}}. \tag{2.4}$$

In a frame of reference attached to the unsteady shock wave, the temporal variation at a point is primarily caused by the turbulent fluctuations being convected by the mean flow. Thus, the time derivative $\partial/\partial t$ is of the order U/ℓ, where U is the characteristic mean velocity. The unsteady term is small compared to the convection across the shock thickness, which scales as U/δ. Thus, the dominant inviscid and viscous terms in (2.3) are

$$\frac{\partial \rho u^{(1)} u^{(1)}}{\partial x^{(1)}} + \frac{\partial p}{\partial x^{(1)}} = \frac{\partial \sigma_{11}}{\partial x^{(1)}}. \tag{2.5}$$

Note that (2.3) and (2.5) are written in a non-inertial frame of reference. There are fictitious force terms of the form $-\rho\xi_{tt}$ on the right-hand side. The instantaneous shock speed ξ_t is assumed to be comparable to the characteristic turbulent velocity fluctuation $\hat{u}$ in magnitude, and the time derivative $\partial/\partial t$ scales as U/ℓ. Thus, the frame acceleration term is of the order $\rho U\hat{u}/\ell$ in magnitude, and its contribution is much smaller than the terms retained in the above equation.

The viscous term in (2.5) is diffusive, and it determines the shock thickness in a Navier–Stokes calculation. An inviscid model, without numerical viscosity, will yield a zero-thickness shock wave. The viscous stress is given in terms of the rate of strain and dynamic viscosity μ of the fluid,

$$\frac{\partial \sigma_{11}}{\partial x^{(1)}} = \frac{4}{3}\mu \frac{\partial^2 u^{(1)}}{\partial x^{(1)} x^{(1)}} + \frac{4}{3}\frac{\partial \mu}{\partial x^{(1)}}\frac{\partial u^{(1)}}{\partial x^{(1)}}, \tag{2.6}$$

where the first terms corresponds to diffusion in constant-property flows and the second term brings in the additional effects due to variation in fluid viscosity. It can be easily seen that the ratio of inertial to viscous terms in (2.5) scales as $\rho U\delta/\mu$, which is taken to be of order unity in magnitude.

It is shown in the Appendix that the viscous terms in the instantaneous vorticity equation follow a similar scaling. Their magnitudes are related to those of the inertial terms via the Reynolds number

$$\frac{\bar{\rho}_1 U\delta}{\bar{\mu}_1} \sim O(1) \tag{2.7}$$

in terms of the characteristic mean flow quantities $\bar{\rho}_1$ and $\bar{\mu}_1$ in the upstream flow and the instantaneous shock thickness. The order-of-magnitude estimates, however, change on time averaging, such that the ratio of inertial to viscous terms in the Reynolds-averaged equation scale as

$$\frac{\bar{\rho}_1 U\bar{\delta}}{\bar{\mu}_1} \sim \frac{\bar{\rho}_1 U\delta}{\bar{\mu}_1}\frac{\bar{\delta}}{\delta} \sim \frac{\bar{\delta}}{\delta} \gg 1, \tag{2.8}$$

where $\bar{\delta}$ (see figure 1) is the mean shock thickness obtained by averaging across a fluctuating shock wave. It is much greater than δ due to unsteady oscillations. The viscous effects in the shock are therefore small in the time-averaged enstrophy equation and are dropped from further analysis. We proceed with the inviscid part of (2.5) and investigate the dominant mechanisms that contribute to enstrophy amplification across the shock wave.

Transforming (2.5) back to the (x, y, z) coordinate system, and collecting terms that are linear in the fluctuations, we get

$$\frac{\partial}{\partial x}\left[2\bar{\rho}\bar{u}(u' - \xi_t)\right] + \frac{\partial}{\partial x}(\rho'\bar{u}^2) + \frac{\partial p'}{\partial x} = 0. \tag{2.9}$$

Once again, the frame acceleration effect $\bar{\rho}\xi_{tt}$ is small compared to the terms retained in the above equation. The linearized Euler equation in an inertial frame of reference is given by

$$\frac{\partial u'}{\partial t} + \bar{u}\frac{\partial u'}{\partial x} + u'\frac{\partial \bar{u}}{\partial x} - \frac{\rho'}{\bar{\rho}^2}\frac{\partial \bar{p}}{\partial x} + \frac{1}{\bar{\rho}}\frac{\partial p'}{\partial x} = 0. \tag{2.10}$$

The unsteady term is retained here because the temporal derivative estimate for the moving frame attached to the shock does not hold. Comparison of this equation with (2.9) yields

$$\frac{\partial u'}{\partial t} \simeq -\xi_t \frac{\partial \bar{u}}{\partial x}. \tag{2.11}$$

A physical interpretation can be deduced by noting that the temporal change at a fixed point in the inertial frame is primarily due to the unsteady shock wave passing through it. The time scale of this variation is given by δ/ξ_t in terms of the instantaneous shock speed and thickness. The corresponding change in the fluid velocity is $u_1 - u_2 \simeq -\Delta\bar{u}$ for an instantaneous shock speed $\xi_t > 0$. Here, Δ represents the jump in a flow variable across the shock. For a shock travelling in the negative x-direction ($\xi_t < 0$), the point of interest will record an opposite velocity change from u_1 to u_2, i.e. $u_2 - u_1 \simeq \Delta\bar{u}$. Noting that the mean flow is steady, we have

$$\frac{\partial u}{\partial t} = \frac{\partial u'}{\partial t} \simeq -\xi_t \frac{\Delta\bar{u}}{\delta} \simeq -\xi_t \frac{\partial \bar{u}}{\partial x}. \tag{2.12}$$

This shows that the streamwise velocity fluctuations measured at a fixed point in the inertial frame are caused by the jump in mean velocity across the shock. Large values of the streamwise normal Reynolds stress in the region of the shock wave are reported in DNS studies (Lee *et al.* 1993; Mahesh *et al.* 1997; Jamme *et al.* 2002; Larsson & Lele 2009), which are an artifact of the unsteady shock motion.

Analysis of the momentum conservation equations of the form (2.3) in the shock-parallel $x^{(2)}$ and $x^{(3)}$ directions yields the corresponding linearized Euler equations for the transverse momenta:

$$\frac{\partial}{\partial x}\left(v' + \bar{u}\xi_y\right) = 0, \tag{2.13}$$

$$\frac{\partial}{\partial x}\left(w' + \bar{u}\xi_z\right) = 0, \tag{2.14}$$

which essentially conserve the fluctuating part of the velocity in the directions tangential to the distorted shock wave.

Differentiating the above equations with respect to z and y respectively results in the following transport equation for $\partial v'/\partial z$ and $\partial w'/\partial y$ across the shock wave:

$$\frac{\partial}{\partial x}\left(\frac{\partial v'}{\partial z}+\bar{u}\xi_{yz}\right)=0, \tag{2.15}$$

$$\frac{\partial}{\partial x}\left(\frac{\partial w'}{\partial y}+\bar{u}\xi_{zy}\right)=0, \tag{2.16}$$

which can be combined to yield an equation for the streamwise component of vorticity $\omega_x'=\partial w'/\partial y-\partial v'/\partial z$:

$$\frac{\partial \omega_x'}{\partial x}=0. \tag{2.17}$$

This states that the streamwise vorticity remains unaltered across the shock in the linear inviscid limit. Identical results have been observed in the work of Mahesh *et al.* (1997).

To obtain a transport equation for the transverse component of vorticity $\omega_z'=\partial v'/\partial x-\partial u'/\partial y$, we differentiate (2.9) with respect to y:

$$\frac{\partial}{\partial x}\left(2\bar{\rho}\bar{u}\frac{\partial u'}{\partial y}\right)-\frac{\partial}{\partial x}\left(2\bar{\rho}\bar{u}\xi_{yt}\right)+\frac{\partial}{\partial x}\left(\frac{\partial \rho'}{\partial y}\bar{u}^2\right)+\frac{\partial^2 p'}{\partial x\partial y}=0, \tag{2.18}$$

which represents the variation of $\partial u'/\partial y$ across the shock. The variation in u' in the transverse direction y is caused by the turbulent fluctuations. The derivative $\partial u'/\partial y$ is therefore of the order $\hat{u}/\ell$ in magnitude and contributes to the turbulent vorticity. The above equation can be written in an equivalent non-conservative form

$$\bar{u}\frac{\partial}{\partial x}\left(\frac{\partial u'}{\partial y}\right)+\frac{\partial u'}{\partial y}\frac{\partial \bar{u}}{\partial x}-\xi_{yt}\frac{\partial \bar{u}}{\partial x}-\frac{\partial \rho'}{\partial y}\frac{1}{\bar{\rho}^2}\frac{\partial \bar{p}}{\partial x}+\frac{1}{\bar{\rho}}\frac{\partial^2 p'}{\partial x\partial y}=0, \tag{2.19}$$

which is similar to the vorticity transport equation derived below. Note that the vorticity equation presented in the Appendix has non-conservative source terms due to vortex stretching and baroclinic torques.

A similar approach of differentiating the linearized y-momentum equation (2.13) with respect to x yields a transport equation for $\partial v'/\partial x$. However, (2.13) is derived by neglecting the spatial derivatives due to turbulent fluctuations in comparison with those due to the shock wave. Therefore, the streamwise derivative of (2.13) yields $\partial v'/\partial x$ that is caused by the shock gradient, and not due to the turbulent fluctuations that contribute to the vorticity component ω_z'. One way to bring in the variation in v' over turbulent length scale ℓ is to consider the time derivative $\partial v'/\partial t$ at a fixed point in space. As noted earlier, the temporal variation is primarily due to turbulent fluctuations being convected by the mean velocity. The shock wave is steady in the frame of reference attached to it, and therefore the shock gradient does not contribute to the time derivative. On differentiating (2.13) with respect to time, we get

$$\frac{\partial}{\partial x}\left(\frac{\partial v'}{\partial t}+\bar{u}\xi_{yt}\right)=0, \tag{2.20}$$

which indicates how $\partial v'/\partial t$ changes across the shock wave.

The rate of change of transverse velocity fluctuations with time at a fixed point in space is given by

$$\frac{\partial v'}{\partial t} = -\bar{u}\frac{\partial v'}{\partial x} - \frac{1}{\bar{\rho}}\frac{\partial p'}{\partial y}. \tag{2.21}$$

This is obtained by collecting the second-order terms in the Euler equation written in the y-direction for a steady one-dimensional mean flow, akin to the one considered in this work. Here, the variations in the flow variables with respect to x and y are due to turbulent fluctuations only and hence over a length scale comparable to ℓ. The spatial derivatives on the right-hand side of (2.21) therefore contribute to the temporal variation in v' due to turbulent fluctuations, and not due to shock gradients. Substituting the above relation in (2.20) yields

$$\bar{u}\frac{\partial}{\partial x}\left(\frac{\partial v'}{\partial x}\right) + \frac{\partial v'}{\partial x}\frac{\partial \bar{u}}{\partial x} - \xi_{yt}\frac{\partial \bar{u}}{\partial x} - \frac{1}{\bar{\rho}^2}\frac{\partial \bar{\rho}}{\partial x}\frac{\partial p'}{\partial y} + \frac{1}{\bar{\rho}}\frac{\partial^2 p'}{\partial x \partial y} = 0, \tag{2.22}$$

which is in a form similar to (2.19), and can be considered as the transport equation for $\partial v'/\partial x$ at the shock.

Combining (2.19) and (2.22) results in

$$\bar{u}\frac{\partial \omega_z'}{\partial x} + \omega_z'\frac{\partial \bar{u}}{\partial x} + \frac{1}{\bar{\rho}^2}\frac{\partial \rho'}{\partial y}\frac{\partial \bar{p}}{\partial x} - \frac{1}{\bar{\rho}^2}\frac{\partial \bar{\rho}}{\partial x}\frac{\partial p'}{\partial y} - \bar{\nu}\frac{\partial^2 \omega_z'}{\partial x^2} = 0, \tag{2.23}$$

which represents the evolution of ω_z' across the shock wave. Note that the viscous diffusion term is added to the equation, as its magnitude is shown (in the Appendix) to be comparable to the other inviscid terms in the equation. Taking a moment with ω_z' and Reynolds averaging yields the equation governing the amplification of $\overline{\omega_z'^2}$ across the shock wave:

$$\bar{u}\frac{\partial}{\partial x}\left(\frac{\overline{\omega_z'^2}}{2}\right) = -\overline{\omega_z'^2}\frac{\partial \bar{u}}{\partial x} - \overline{\omega_z'\rho'_{,y}}\frac{1}{\bar{\rho}^2}\frac{\partial \bar{p}}{\partial x} + \overline{\omega_z' p'_{,y}}\frac{1}{\bar{\rho}^2}\frac{\partial \bar{\rho}}{\partial x} + \bar{\nu}\frac{\partial^2}{\partial x^2}\left(\frac{\overline{\omega_z'^2}}{2}\right) - \bar{\nu}\overline{\frac{\partial \omega_z'}{\partial x}\frac{\partial \omega_z'}{\partial x}}. \tag{2.24}$$

The other transverse vorticity component $\overline{\omega_y'^2}$ follows a very similar equation. The viscous diffusion and dissipation effects are argued (see the Appendix) to be small compared to the inviscid terms in the above time-averaged equation. The dominant mechanisms contributing to the amplification of enstrophy $\overline{\omega_i'\omega_i'} = \overline{\omega_x'^2} + \overline{\omega_y'^2} + \overline{\omega_z'^2}$ across the shock are thus given by

$$\bar{u}\frac{\partial \overline{\omega_i'\omega_i'}}{\partial x} = -4\overline{\omega_z'^2}\frac{\partial \bar{u}}{\partial x} - 4\overline{\omega_z'\rho'_{,y}}\frac{1}{\bar{\rho}^2}\frac{\partial \bar{p}}{\partial x} + 4\overline{\omega_z' p'_{,y}}\frac{1}{\bar{\rho}^2}\frac{\partial \bar{\rho}}{\partial x}, \tag{2.25}$$

obtained by combining (2.17) in the streamwise direction with those in the transverse directions of the form (2.24). A symmetry about the shock-normal direction means that $\overline{\omega_z'^2} = \overline{\omega_y'^2}$, $\overline{\omega_z'\rho'_{,y}} = \overline{\omega_y'\rho'_{,z}}$ and $\overline{\omega_z' p'_{,y}} = \overline{\omega_y' p'_{,z}}$.

The first term on the right-hand side of (2.25) is the production due to bulk compression, and the other two terms correspond to the baroclinic generation of vorticity. These terms are denoted by P_ω, B_ω^1 and B_ω^2 respectively. Consider a fluid element passing through the shock. Vorticity can be interpreted as the rotation of the fluid element. Bulk compression at the shock compresses the fluid element and thus reduces its moment of inertia. This is manifested as an increase in the rotation of the fluid element, and equivalently as an increase in its vorticity behind the shock.

The baroclinic source terms arise due to a mis-alignment of the pressure-gradient and density-gradient vectors. The sign of the correlations between the fluctuating vorticity and the gradient in density and pressure fluctuations determines whether these terms have an amplifying effect on vorticity or they damp vorticity fluctuations.

The enstrophy equation (2.25) does not have any contribution from the shock deformation, denoted by ξ. The local shock speed ξ_t is found to affect the streamwise velocity fluctuations in (2.9), and the angular distortion ξ_y and ξ_z alter the transverse velocity components in (2.13) and (2.14). It is shown by Sinha *et al.* (2003) that the correlation $\overline{u'\xi_t}$ has a damping effect on the streamwise Reynolds stress and terms of the form $\overline{v'\xi_y}$ and $\overline{w'\xi_z}$ enhance the transverse Reynolds stresses across a shock wave. The equations for $\partial u'/\partial y$ and $\partial v'/\partial x$ presented above have a contribution due to ξ_{yt}, which is the time rate of change of the shock angle. The corresponding terms cancel each other in (2.23) such that there is no net effect on the vorticity fluctuations. Thus, the unsteady shock deformation has no direct influence on the amplification of vorticity fluctuations across a shock wave, as long as the fluctuations and the shock distortions are small, and the linear analysis is valid.

2.1. *Integrated form of equations*

The flow variables across the shock are related by the Rankine–Hugoniot jump conditions. These relations can be obtained by integrating the conservation equations of the form (2.5) across the shock. The integrated contributions of the viscous terms are small, as noted below. On writing these equations for an unsteady shock wave and linearizing them about the mean flow yields the following relations for the fluctuating quantities:

$$2\bar{\rho}_1\bar{u}_1(u_2' - u_1') + \rho_2'\bar{u}_2^2 - \rho_1'\bar{u}_1^2 + p_2' - p_1' = 0, \tag{2.26}$$

$$v_2' - v_1' + \xi_y(\bar{u}_2 - \bar{u}_1) = 0, \tag{2.27}$$

$$w_2' - w_1' + \xi_z(\bar{u}_2 - \bar{u}_1) = 0, \tag{2.28}$$

where subscripts 1 and 2 denote shock upstream and downstream locations. These equations can be interpreted as the integrated form of (2.9), (2.13) and (2.14), where the streamwise derivatives across the shock are replaced by the corresponding differences between the upstream and downstream values. The inviscid terms in (2.26) scale as $\bar{\rho}_1 U\hat{u}$, whereas the leading viscous terms are of the order $\bar{\mu}_1\hat{u}/\ell$ in magnitude. Their ratio $\bar{\rho}_1 U\ell/\bar{\mu}_1$ is much larger than unity, due to the fact that $\delta \ll \ell$ and $\bar{\rho}_1 U\delta/\bar{\mu}_1 = O(1)$. The viscous and inviscid terms in (2.27) and (2.28) exhibit a similar trend. The viscous effects are therefore dropped from the above equations.

Using (2.26)–(2.28) as the starting point and following the same procedure as above, we arrive at an integrated form of (2.25). The steps are delineated next. Writing (2.26) in an equivalent form

$$\bar{u}_1(u_2' - u_1') + (u_1' - \xi_t)(\bar{u}_2 - \bar{u}_1) - \frac{\rho_1'}{\bar{\rho}_1^2}(\bar{p}_2 - \bar{p}_1) + \frac{p_2' - p_1'}{\bar{\rho}_1} = 0 \tag{2.29}$$

and differentiating it with respect to y, we get an equation relating $\partial u'/\partial y$ on each side of the shock wave:

$$\bar{u}_1\left(\frac{\partial u_2'}{\partial y} - \frac{\partial u_1'}{\partial y}\right) + \frac{\partial u_1'}{\partial y}(\bar{u}_2 - \bar{u}_1) - \xi_{yt}(\bar{u}_2 - \bar{u}_1) - \frac{\partial \rho_1'}{\partial y}\frac{\bar{p}_2 - \bar{p}_1}{\bar{\rho}_1^2} + \frac{1}{\bar{\rho}_1}\left(\frac{\partial p_2'}{\partial y} - \frac{\partial p_1'}{\partial y}\right) = 0. \tag{2.30}$$

A similar equation relating $\partial v'/\partial x$ on each side of the shock wave cannot be directly obtained by differentiating (2.27) with respect to x. Care is to be taken so as to retain contributions from turbulent fluctuations, and not by the shock gradient, to enstrophy. As earlier, we consider the linearized Euler equation for the y-momentum on each side of the shock wave. The x-derivative at the shock is then written as the difference between the upstream and downstream equations:

$$\left(\frac{\partial v_2'}{\partial t} + \bar{u}_2\frac{\partial v_2'}{\partial x} + \frac{1}{\bar{\rho}_2}\frac{\partial p_2'}{\partial y}\right) - \left(\frac{\partial v_1'}{\partial t} + \bar{u}_1\frac{\partial v_1'}{\partial x} + \frac{1}{\bar{\rho}_1}\frac{\partial p_1'}{\partial y}\right) = 0. \tag{2.31}$$

This is similar to the procedure followed by Kevlahan (1997). The shock-normal derivatives are termed 'external' and are evaluated by writing the conservation equations on each side of the shock wave. The difference between the upstream and downstream equations yields the jump in the shock-normal velocity gradient that contributes to the vorticity amplification at the shock wave.

The jump relation (2.31), when combined with the temporal derivative of (2.27), results in

$$\bar{u}_2\frac{\partial v_2'}{\partial x} - \bar{u}_1\frac{\partial v_1'}{\partial x} - \xi_{yt}(\bar{u}_2 - \bar{u}_1) + \frac{1}{\bar{\rho}_2}\frac{\partial p_2'}{\partial y} - \frac{1}{\bar{\rho}_1}\frac{\partial p_1'}{\partial y} = 0, \tag{2.32}$$

which relates $\partial v'/\partial x$ on each side of the shock wave. Combining (2.30) and (2.32) gives the following equation for the change in transverse vorticity fluctuations across the shock:

$$\bar{u}_1(\omega_{z2}' - \omega_{z1}') = -\omega_{z2}'\Delta\bar{u} - \rho_{1,y}'\frac{\Delta\bar{p}}{\bar{\rho}_1^2} + p_{2,y}'\frac{\Delta\bar{\rho}}{\bar{\rho}_1\bar{\rho}_2} - (u_{2,y}' - u_{1,y}')\Delta\bar{u}, \tag{2.33}$$

where $\Delta\bar{u} = \bar{u}_2 - \bar{u}_1$, $\Delta\bar{p} = \bar{p}_2 - \bar{p}_1$ and $\Delta\bar{\rho} = \bar{\rho}_2 - \bar{\rho}_1$. The above equation can be treated as the integrated form of (2.23) without the viscous terms.

Multiplying both sides by $\omega_{zm}' = (1/2)(\omega_{z1}' + \omega_{z2}')$ and Reynolds averaging yields

$$\begin{aligned}\bar{u}_1\frac{(\overline{\omega_{z2}'^2} - \overline{\omega_{z1}'^2})}{2} = &-\overline{\omega_{zm}'\omega_{z2}'}\Delta\bar{u} - \overline{\omega_{zm}'\rho_{1,y}'}\frac{\Delta\bar{p}}{\bar{\rho}_1^2} \\ &+ \overline{\omega_{zm}'p_{2,y}'}\frac{\Delta\bar{\rho}}{\bar{\rho}_1\bar{\rho}_2} - \overline{\omega_{zm}'(u_{2,y}' - u_{1,y}')}\Delta\bar{u},\end{aligned} \tag{2.34}$$

which can be interpreted as the integrated form of (2.24) across the shock wave. A similar equation can be derived for the other transverse vorticity component. Further, it can be easily shown using (2.27) and (2.28) that the streamwise vorticity component remains unchanged across the shock wave. Combining all the components yields

$$\begin{aligned}\bar{u}_1\left[(\overline{\omega_i'\omega_i'})_2 - (\overline{\omega_i'\omega_i'})_1\right] = &-4\overline{\omega_{zm}'\omega_{z2}'}\Delta\bar{u} - 4\overline{\omega_{zm}'\rho_{1,y}'}\frac{\Delta\bar{p}}{\bar{\rho}_1^2} \\ &+ 4\overline{\omega_{zm}'p_{2,y}'}\frac{\Delta\bar{\rho}}{\bar{\rho}_1\bar{\rho}_2} - 4\overline{\omega_{zm}'(u_{2,y}' - u_{1,y}')}\Delta\bar{u},\end{aligned} \tag{2.35}$$

which is the integrated version of the enstrophy equation (2.25) at the shock wave.

The first term on the right-hand side represents production due to bulk compression, and the second and third terms correspond to the baroclinic generation of vorticity. The last term arises due to differencing across the shock, and it does not have a counterpart in (2.25). Once again the shock-unsteadiness and distortion mechanisms do not affect the enstrophy jump in (2.35).

2.2. *Budget of enstrophy amplification*

A budget of the enstrophy equation (2.35) is computed using results from the LIA of Mahesh *et al.* (1997). The upstream turbulence field is represented as a collection of two-dimensional vorticity–entropy waves. The velocity and thermodynamic fluctuations associated with a single wave are given by

$$\frac{u_1'}{\bar{u}_1} = A_v \sin\psi \exp[\mathrm{i}\kappa(x\cos\psi + y\sin\psi - \bar{u}_1 t\cos\psi)], \tag{2.36a}$$

$$\frac{v_1'}{\bar{u}_1} = -A_v \cos\psi \exp[\mathrm{i}\kappa(x\cos\psi + y\sin\psi - \bar{u}_1 t\cos\psi)], \tag{2.36b}$$

$$\frac{\rho_1'}{\bar{\rho}_1} = -\frac{T_1'}{\bar{T}_1} = A_e \exp[\mathrm{i}\kappa(x\cos\psi + y\sin\psi - \bar{u}_1 t\cos\psi)], \tag{2.36c}$$

$$\frac{p_1'}{\bar{p}_1} = 0, \tag{2.36d}$$

where κ is the wavenumber magnitude and ψ is the angle between the wavenumber vector and the mean shock-normal direction. A_v represents the magnitude of the solenoidal velocity fluctuations and A_e corresponds to the entropy mode. The ratio A_e/A_v is defined as $A_r \mathrm{e}^{\mathrm{i}\phi_r}$, where A_r is the amplitude ratio and ϕ_r is the phase difference between the entropy and vorticity components. It can be shown that $A_r \mathrm{e}^{\mathrm{i}\phi_r} = A_{uT}\sin\psi$, such that $\phi_r = 0$ for the positive A_{uT} values considered in this work, while negative A_{uT} values correspond to $\phi_r = \pi$. In both cases, the $\sin\psi$ functional dependence results in an axisymmetric entropy field for an isotropic vortical flow.

The interaction of a vorticity–entropy wave with a shock generates vortical, entropy and acoustic components downstream of the shock wave. The resultant flow variables are computed by applying the linearized Rankine–Hugoniot equations at the shock and solving the linearized Euler equations in the downstream flow. Superposition of the waves, for a given upstream energy spectrum, yields the turbulence statistics behind the shock. The flow variables immediately downstream of the shock (subscript 2) are used along with the prescribed upstream values (subscript 1) to compute a budget of (2.35). The terms on the right-hand side are evaluated to assess the contribution of the different physical mechanisms towards the amplification of vorticity fluctuations at the shock wave. The data are normalized by $\bar{u}_1^3\kappa_0^2$, where κ_0 is the most energetic wavenumber, and are plotted as a function of upstream Mach number for different A_{uT} values (see figure 2).

The production due to mean compression has a dominant effect on the amplification of vorticity fluctuations across the shock wave. This is true for all Mach numbers and for all the A_{uT} cases presented in figure 2. In the absence of upstream entropy fluctuations ($A_{uT} = 0$), the baroclinic term B_ω^1 is identically zero at all Mach numbers. For $A_{uT} > 0$, B_ω^1 is positive and its magnitude increases rapidly with the level of temperature fluctuations in the incoming flow. For high values of A_{uT} (e.g. in figure 2*e*), B_ω^1 is a major contributor to vorticity amplification across the shock. On the other hand, B_ω^1 has a damping effect on the vorticity fluctuations for $A_{uT} < 0$ (see figure 2*f*). The other baroclinic source term B_ω^2 is found to be negative for all values of A_{uT}. The last term E_ω has minimal effect on the vorticity budget across the shock wave.

The amplifying effect of B_ω^1 in (2.35) for $A_{uT} > 0$ is due to a negative correlation between fluctuating vorticity and density fluctuation gradient, i.e. the two quantities

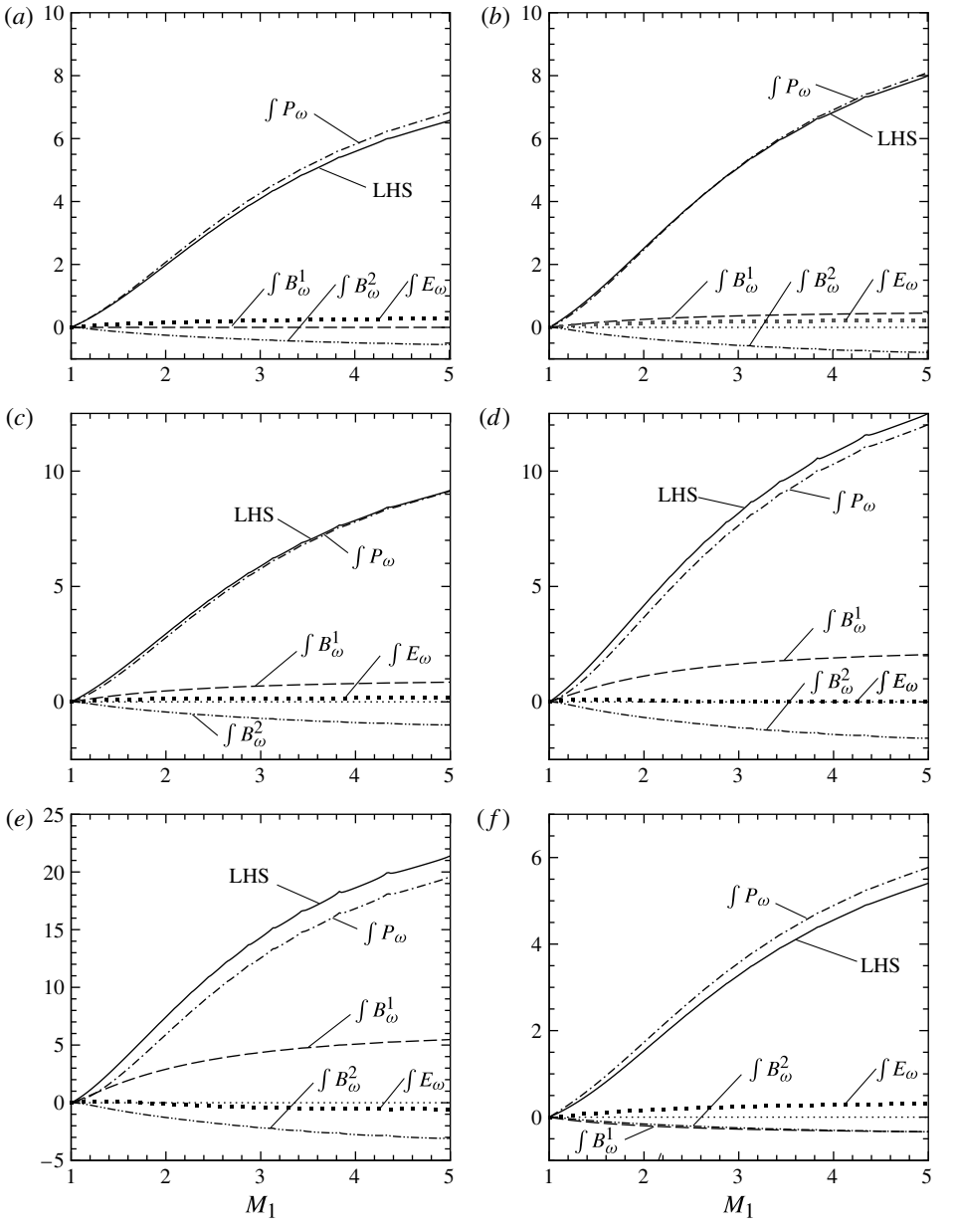

FIGURE 2. Budget of enstrophy amplification as a function of upstream Mach number for different values of A_{uT}. (*a*) $A_{uT} = 0$; (*b*) $A_{uT} = 0.58$; (*c*) $A_{uT} = 1.0$; (*d*) $A_{uT} = 2.0$; (*e*) $A_{uT} = 4.0$; (*f*) $A_{uT} = -0.58$. Here, $\int P_\omega$, $\int B^1_\omega$, $\int B^2_\omega$ and $\int E_\omega$ represent the four terms on the right-hand side of (2.35). The amplification of enstrophy on the left-hand side is denoted by LHS, where all the terms are normalized by $\bar{u}_1^3 \kappa_0^2$.

are out of phase. A physical interpretation of the underlying phenomenon is shown graphically by Mahesh *et al.* (1997). For the case when $\omega_z' > 0$ (counter-clockwise) and $\rho_{,y}' < 0$, there is a downward shift of the centre of mass of a fluid element. The mean pressure gradient acting at the geometric centre thus results in a

counter-clockwise moment about the centre of mass. The baroclinic torque therefore adds to the vorticity of the fluid element. Similarly, for $\omega_z' < 0$ (clockwise) and $\rho_{,y}' > 0$, the pressure gradient at the geometric centre creates a clockwise moment about the centre of mass, which is now shifted upwards. In both cases, the baroclinic torque has an amplifying effect on the vorticity fluctuation. The opposite is true for $A_{uT} < 0$, where the vorticity fluctuations and the density fluctuation gradient are in phase, i.e. $\overline{\omega_z' \rho_{,y}'} > 0$. Arguments similar to those given above can be advanced to show that the baroclinic torque in this case is opposed to the direction of the vorticity fluctuations. This results in a damping effect due to B_ω^1.

The second baroclinic source term B_ω^2 in (2.35) brings in the effect of pressure fluctuations on vorticity amplification. It is found that the fluctuating vorticity is out of phase with the pressure fluctuation gradient, i.e. $\overline{\omega_z' p_{,y}'} < 0$, irrespective of the sign of A_{uT}. For the case where $\omega_z' > 0$ (counter-clockwise) and $p_{,y}' < 0$, the centre of pressure is shifted downwards. The net pressure force thus has a clockwise moment about the centre of mass located at the geometric centre of the fluid element. The baroclinic torque therefore opposes the fluid vorticity direction. A similar opposing effect of the baroclinic torque on the vorticity fluctuation can also be shown in the case where $\omega_z' < 0$ and $p_{,y}' > 0$. The corresponding source term B_ω^2 has a negative contribution to the vorticity budget for all values of A_{uT}.

Larsson & Lele (2009) present DNS of homogeneous isotropic turbulence interacting with nominally normal shock waves. Data from their DNS are used to compute the dominant terms in (2.35) and the results are presented in figure 3. The corresponding terms obtained from linear theory results are reproduced from figure 2(*a*) for comparison. The Mach 1.5, 2.5, 3.5 and 4.7 cases with $M_t = 0.22$ and $A_{uT} \simeq 0$ (see table 1 in § 4) are considered. The locations 1 and 2 are identified upstream and downstream of the time-averaged shock wave, and averaging is done over the transverse directions. The left-hand side and production terms in (2.35) computed using DNS data follow the qualitative trends obtained from linear theory. There are, however, quantitative differences between the LIA and DNS results, as described below.

The integrated value of the production term in (2.35) is computed as

$$\int P_\omega = -4\overline{\omega_{zm}' \omega_{z2}'} \Delta \bar{u} = 2(\overline{\omega_{z1}' \omega_{z2}'} + \overline{\omega_{z2}'^2})|\Delta \bar{u}|. \tag{2.37}$$

It is found that the first part has negligible contribution to the vorticity generation, due to a vanishingly small correlation between the vorticity fluctuations across the mean shock gradient. This is a consequence of the viscous and nonlinear processes occurring in this region of thickness $\bar{\delta}$, which is comparable to the turbulent length scale ℓ in magnitude. The absence of viscous and nonlinear effects in LIA yields a strong correlation between the vorticity fluctuations immediately upstream and downstream of the shock wave. Both correlations in (2.37) contribute to the production of vorticity, which is comparable to the enstrophy amplification term (marked as left-hand side) as linear theory estimates. On the other hand, the production term computed using the DNS data is lower than the corresponding left-hand-side term in magnitude (see figure 3).

Both LIA and DNS data show that the production due to mean compression has a dominant effect on enstrophy amplification for $A_{uT} = 0$. At $M_1 = 2.5$, the production accounts for $\sim 80\,\%$ of the enstrophy amplification in the DNS, and its contribution is even higher at higher Mach numbers. The production term is therefore the subject of further analysis and modelling for interactions without appreciable

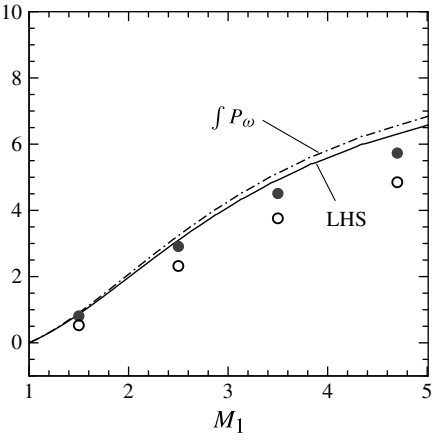

FIGURE 3. The dominant terms in the enstrophy budget computed from LIA results (lines) for $A_{uT} = 0$ and using DNS data (symbols) of Larsson & Lele (2009): •, left-hand side; and ∘, production term in (2.35), where the DNS data are scaled to match the upstream enstrophy level in the linear theory.

velocity–temperature correlation upstream of the shock wave. A similar evaluation of the source terms for non-zero A_{uT} cases using the corresponding DNS data, if available, can quantify the contribution of the baroclinic torques to the enstrophy jump in the presence of nonlinear and viscous effects.

3. Modelling of the enstrophy equation

In this section, models are developed for the unclosed terms in the enstrophy equation (2.25). The inviscid mechanisms that play a dominant role in enstrophy amplification at the shock are considered here. The viscous diffusion and dissipation terms are assumed to be relatively small (see the Appendix). The model predictions may therefore apply to high-Reynolds-number ($U\bar{\delta}/\nu \gg 1$) flows, and are compared with LIA results based on linearized Euler equations. First, the case of purely vortical turbulence upstream of the shock wave is studied. This is followed by modelling the effect of upstream temperature fluctuations.

3.1. *Modelling for* $A_{uT} = 0$

Based on the budget of the enstrophy equation for $A_{uT} = 0$ presented above, the transport equation for $\overline{\omega_i'\omega_i'}$ is approximated as

$$\bar{u}\frac{\partial \overline{\omega_i'\omega_i'}}{\partial x} \simeq -4\overline{\omega_z'^2}\frac{\partial \bar{u}}{\partial x} = -c_\omega\, \overline{\omega_i'\omega_i'}\frac{\partial \bar{u}}{\partial x}, \tag{3.1}$$

where the viscous terms are neglected and the parameter c_ω is used to model the production term. Integration across the mean shock thickness yields a closed-form solution for $\overline{\omega_i'\omega_i'}$ amplification across the shock wave:

$$\frac{(\overline{\omega_i'\omega_i'})_2}{(\overline{\omega_i'\omega_i'})_1} = \left(\frac{\bar{u}_1}{\bar{u}_2}\right)^{c_\omega}. \tag{3.2}$$

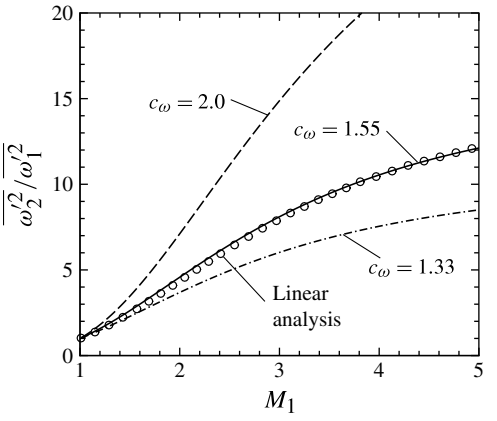

FIGURE 4. $\overline{\omega_i'\omega_i'}$-amplification across a normal shock when $A_{uT} = 0$. Model predictions (lines) are compared with linear theory results (circles).

Assuming isotropic turbulence, $\overline{\omega_x'^2} = \overline{\omega_y'^2} = \overline{\omega_z'^2} = \overline{\omega_i'\omega_i'}/3$ yields $c_\omega = 4/3$, and the results are compared to the enstrophy amplification obtained from LIA in figure 4. The model predictions compare well with the theoretical values for low upstream Mach number, but are lower than the theory at higher Mach numbers.

The model can be improved by noting that ω_y' and ω_z' are amplified across the shock, while ω_x' remains relatively unchanged. This may result in $\overline{\omega_x'^2} \ll \overline{\omega_y'^2} = \overline{\omega_z'^2} \simeq \overline{\omega_i'\omega_i'}/2$ downstream of the shock wave. Using this estimate of $\overline{\omega_z'^2}$ in (3.1) yields $c_\omega = 2$, which is found to over-predict enstrophy amplification in figure 4. In fact, $\overline{\omega_i'\omega_i'}/3 \leqslant \overline{\omega_z'^2} \leqslant \overline{\omega_i'\omega_i'}/2$ such that the above values may be regarded as the lower and upper limits for c_ω. The actual value lies somewhere in between the two extremes. A value of $c_\omega = 1.55$ matches the theoretical results in figure 4 closely.

3.2. *Modelling for non-zero A_{uT}*

The budget of the enstrophy equation shows that the baroclinic source term

$$B_\omega^1 = -4\overline{\omega_z'\rho_{,y}'}\frac{1}{\bar{\rho}^2}\frac{\partial \bar{p}}{\partial x} = 4\overline{\omega_z'\rho_{,y}'}\frac{\bar{u}}{\bar{\rho}}\frac{\partial \bar{u}}{\partial x} \tag{3.3}$$

is important for $A_{uT} \neq 0$ cases. It is positive for $A_{uT} > 0$ and vice-versa. In the following, the unclosed correlation $\overline{\omega_z'\rho_{,y}'}$ is modelled such that the effect of B_ω^1 can be included in the modelled equation.

In the absence of pressure fluctuations in the upstream flow, the density fluctuations are generated by the entropy component. The thermodynamic fluctuations are related to the vortical part via A_{uT}, as in (1.2). For a vorticity–entropy wave considered in the LIA (see § 2.2), it can be shown that

$$\frac{\rho_{1,y}'}{\bar{\rho}_1} = -A_{uT}\frac{\omega_{z1}'\sin^2\psi}{\bar{u}_1}. \tag{3.4}$$

On integration over the energy spectrum, we get the following relation for the upstream turbulence field:

$$\frac{\overline{\omega'_{z1}\rho'_{1,y}}}{\bar{\rho}_1} = -A_{uT}\frac{\overline{\omega'^2_{z1}\sin^2\psi}}{\bar{u}_1} = -b_\omega A_{uT}\frac{\overline{\omega'^2_{z1}}}{\bar{u}_1}, \tag{3.5}$$

where b_ω is a modelling coefficient and its value is found to be $1/2$ using linear analysis results.

Based on the foregoing, the baroclinic term can be modelled as

$$B^1_\omega = 4\overline{\omega'_z\rho'_{,y}}\frac{\bar{u}}{\bar{\rho}}\frac{\partial\bar{u}}{\partial x} = -4b_\omega A_{uT}\overline{\omega'^2_z}\frac{\partial\bar{u}}{\partial x}. \tag{3.6}$$

Combining this with the model for the production term (3.1) yields

$$\bar{u}\frac{\partial\overline{\omega'_i\omega'_i}}{\partial x} \simeq -4(1+b_\omega A_{uT})\overline{\omega'^2_z}\frac{\partial\bar{u}}{\partial x} = -c_\omega(1+b_\omega A_{uT})\overline{\omega'_i\omega'_i}\frac{\partial\bar{u}}{\partial x}, \tag{3.7}$$

where the viscous terms are once again neglected in the equation. The amplification in $\overline{\omega'_i\omega'_i}$ across the shock in the high-Reynolds-number limit is therefore given by

$$\frac{(\overline{\omega'_i\omega'_i})_2}{(\overline{\omega'_i\omega'_i})_1} = \left(\frac{\bar{u}_1}{\bar{u}_2}\right)^{c_\omega(1+b_\omega A_{uT})}, \tag{3.8}$$

and it is compared to LIA results for different values of A_{uT} in figure 5. The prediction for $A_{uT}=0$ is identical to that presented earlier. For $A_{uT}=0.58$, the above equation matches theoretical values for Mach numbers less than 1.2, but over-predicts the amplification at higher M_1. The over-amplification of enstrophy at high Mach numbers increases dramatically for $A_{uT}=1$, 2 and 4. The model predicts the damping effect of B^1_ω for negative A_{uT} (see figure 5*a*), but yields too low a value of $\overline{\omega'_i\omega'_i}$-amplification at high Mach numbers.

Next, we attempt to improve the modelling of B^1_ω. Instead of using the upstream closure given by (3.5), taking an average of upstream and downstream values may give a better estimate. Thus,

$$\begin{aligned}\frac{\overline{\omega'_z\rho'_{,y}}}{\overline{\omega'^2_z}}\frac{\bar{u}}{\bar{\rho}} &\simeq \frac{1}{2}\left[\frac{\overline{\omega'_{z1}\rho'_{1,y}}}{\overline{\omega'^2_{z1}}}\frac{\bar{u}_1}{\bar{\rho}_1} + \frac{\overline{\omega'_{z2}\rho'_{2,y}}}{\overline{\omega'^2_{z2}}}\frac{\bar{u}_2}{\bar{\rho}_2}\right]\\ &= -\frac{b_\omega A_{uT}}{2}\left[1+\left(\frac{\overline{\omega'_{z2}\rho'_{2,y}}}{\overline{\omega'^2_{z2}}}\frac{\bar{u}_2}{\bar{\rho}_2}\right)\left(\frac{\overline{\omega'_{z1}\rho'_{1,y}}}{\overline{\omega'^2_{z1}}}\frac{\bar{u}_1}{\bar{\rho}_1}\right)^{-1}\right]\end{aligned} \tag{3.9}$$

where the downstream correlation is evaluated immediately behind the shock, so as to consider the effect in the vicinity of the shock wave. The downstream term is found to be smaller in magnitude than the upstream correlation for high values of M_1. This is mainly because amplification of the transverse vorticity $\overline{\omega'^2_z}$ across a strong shock wave is larger than that of $\overline{\omega'_z\rho'_{,y}}$. An increase in the mean density and a corresponding decrease in the mean velocity add to this effect. The ratio of the upstream and downstream correlations is plotted in figure 6 for different values of A_{uT}. It has values close to 1 for $M_1\to 1$ and tends to low values for high upstream Mach number. This

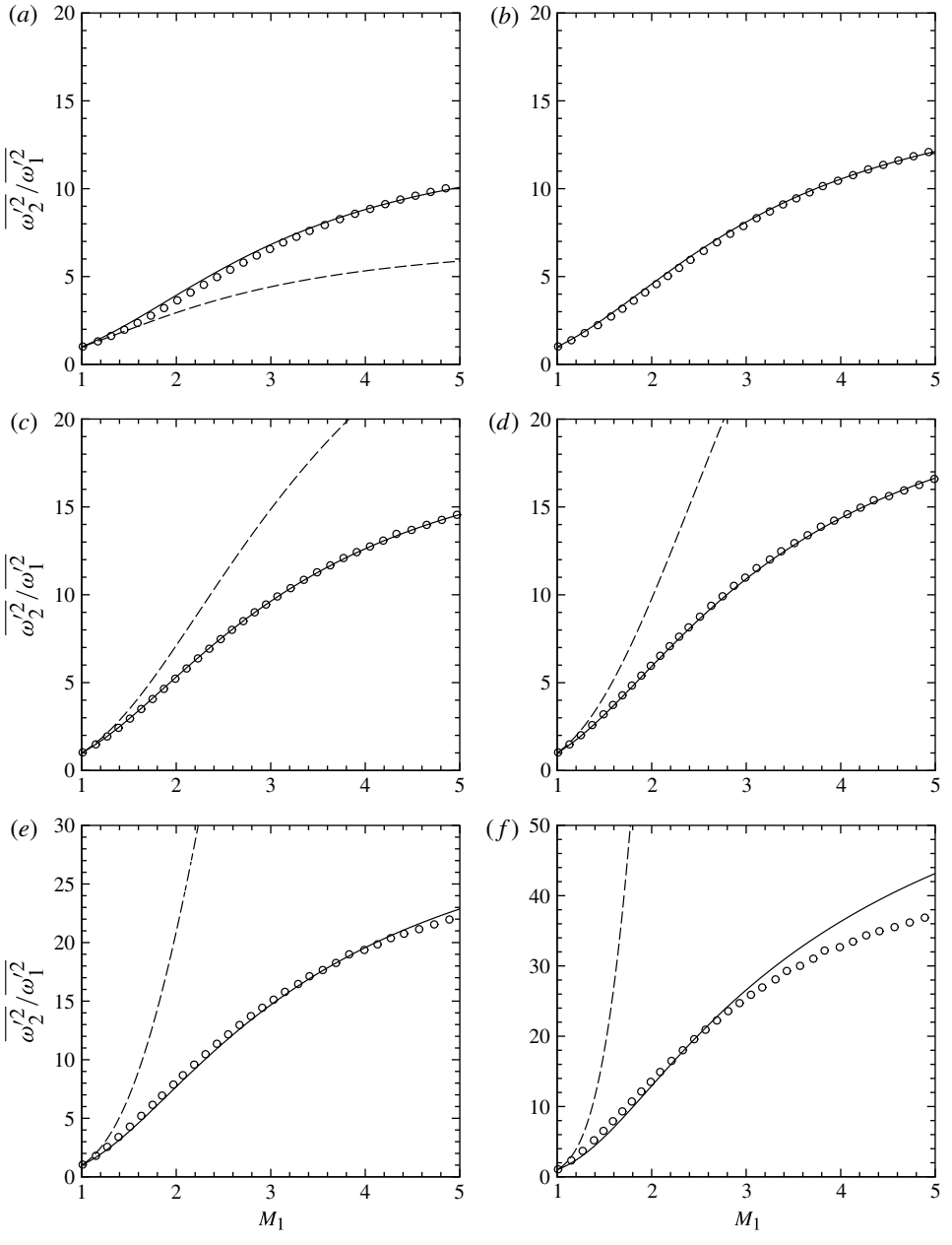

FIGURE 5. Model predictions for $\overline{\omega_i'\omega_i'}$-amplification across a normal shock for different values of A_{uT} are compared with LIA results (symbols). The dashed line represents (3.8) and the solid line corresponds to (3.11). (*a*) $A_{uT} = -0.58$; (*b*) $A_{uT} = 0$; (*c*) $A_{uT} = 0.58$; (*d*) $A_{uT} = 1.0$; (*e*) $A_{uT} = 2.0$; (*f*) $A_{uT} = 4.0$.

trend can be mimicked by a factor $\exp(1 - M_1)$, such that

$$\frac{\overline{\omega_z'\rho_{,y}'}}{\overline{\omega_z'^2}}\frac{\bar{u}}{\bar{\rho}} \simeq -\frac{b_\omega A_{uT}}{2}[1 + \mathrm{e}^{1-M_1}]. \tag{3.10}$$

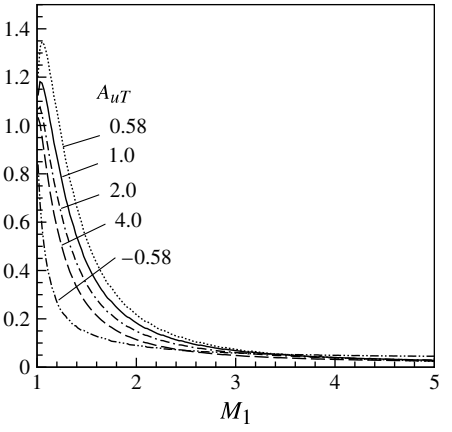

FIGURE 6. Ratio of downstream to upstream values of the correlations $(\overline{\omega_z'\rho_{,y}'}/\overline{\omega_z'^2})(\bar{u}/\bar{\rho})$ as computed using linear theory.

The above modification can be incorporated in the model equation (3.6) for B_ω^1 by multiplying b_ω by $(1/2)[1 + \mathrm{e}^{1-M_1}]$. The term $(1/2)[1 + \mathrm{e}^{1-M_1}] \simeq 1$ at low supersonic M_1, and decreases to $1/2$ at high Mach numbers. It therefore reduces the amplifying effect of A_{uT}, especially for high M_1, and results in an improvement in the model predictions. However, the discrepancy between model and theory is still considerable for large values of A_{uT}. Including an additional factor of $1/2$ results in a good match with theory for all cases (see figure 5), except for $A_{uT} = 4$ and $M_1 > 3$. This reduction in the model coefficient by $1/2$ may be interpreted as bringing in the effect of B_ω^2, which has a negative contribution to the budget (see figure 2).

Thus, the final modelled form of the production and baroclinic terms in the enstrophy equation can be written as

$$\bar{u}\frac{\partial\overline{\omega_i'\omega_i'}}{\partial x} \simeq -c_\omega(1 + b_\omega' A_{uT})\overline{\omega_i'\omega_i'}\frac{\partial\bar{u}}{\partial x} \tag{3.11}$$

with

$$b_\omega' = \tfrac{1}{4}b_\omega[1 + \mathrm{e}^{1-M_1}]. \tag{3.12}$$

4. Model evaluation

The model developed above is applied to the interaction of homogeneous isotropic turbulence with a normal shock. As noted earlier, the solenoidal dissipation rate can be written as $\epsilon_s = \bar{\nu}\overline{\omega_i'\omega_i'}$. The modelled enstrophy equation is cast in the framework of a k–ϵ turbulence model, and viscous dissipation is added to simulate turbulence decay on each side of the shock wave. The resulting equations are used to compute shock/homogeneous turbulence interaction cases, for which DNS data are available in literature.

4.1. *Model for the solenoidal dissipation rate*

Amplification of the solenoidal dissipation rate across the shock can be expressed in terms of the changes in the kinematic viscosity and the amplification in

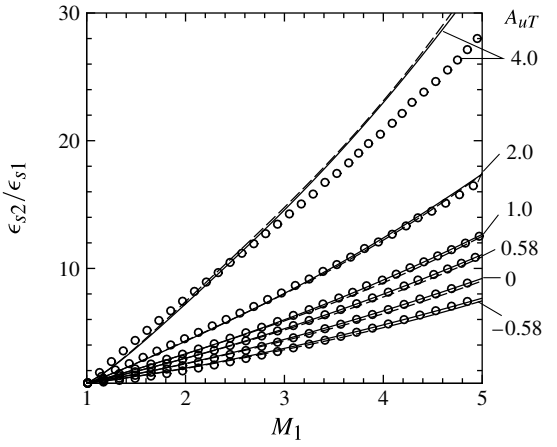

FIGURE 7. Amplification of the solenoidal dissipation rate predicted by model equations (4.3), solid line, and (4.10), dashed line, are compared with linear theory results, shown by symbols.

enstrophy:

$$\bar{u}\frac{\partial \epsilon_s}{\partial x} = \bar{u}\frac{\partial}{\partial x}(\bar{\nu}\overline{\omega_i'\omega_i'}) = \bar{u}\overline{\omega_i'\omega_i'}\frac{\partial \bar{\nu}}{\partial x} + \bar{u}\bar{\nu}\frac{\partial \overline{\omega_i'\omega_i'}}{\partial x}. \tag{4.1}$$

The dynamic viscosity $\bar{\mu}$ is assumed to be a function of mean temperature $\bar{T}$, such that $\bar{\mu} = c\bar{T}^{\alpha}$. Here c and $\alpha = 0.76$ are constants. The change in kinematic viscosity across the shock can be calculated as

$$\frac{\partial \bar{\nu}}{\partial x} = -\frac{\bar{\mu}}{\bar{\rho}^2}\frac{\partial \bar{\rho}}{\partial x} + \frac{1}{\bar{\rho}}\frac{\partial \bar{\mu}}{\partial x} = \bar{\nu}\left[\frac{1}{\bar{u}}\frac{\partial \bar{u}}{\partial x} + \frac{\alpha}{\bar{T}}\frac{\partial \bar{T}}{\partial x}\right]. \tag{4.2}$$

Combining (3.11) and (4.2) yields the following modelled equation for ϵ_s:

$$\bar{u}\frac{\partial \epsilon_s}{\partial x} \simeq -c_\omega(1 + b'_\omega A_{uT})\epsilon_s\frac{\partial \bar{u}}{\partial x} + \epsilon_s\frac{\partial \bar{u}}{\partial x} + \alpha\epsilon_s\frac{\bar{u}}{\bar{T}}\frac{\partial \bar{T}}{\partial x}, \tag{4.3}$$

where the first term models the effect of mean compression and baroclinic torques on enstrophy amplification, and the last two terms are due to the changes in mean kinematic viscosity. Similarly to (3.11), the above equation neglects viscous effects and the model predictions can be assumed to hold for high-Reynolds-number flows. Integrating it across the shock wave yields

$$\frac{\epsilon_{s2}}{\epsilon_{s1}} = \left(\frac{\bar{T}_2}{\bar{T}_1}\right)^{\alpha}\left(\frac{\bar{u}_1}{\bar{u}_2}\right)^{c_\omega(1+b'_\omega A_{uT})-1}, \tag{4.4}$$

which matches linear theory results for all M_1 and A_{uT} (see figure 7), except for the $A_{uT} = 4$ case when $M_1 > 3$.

The conservation of total enthalpy across a normal shock

$$\frac{\bar{u}}{\bar{T}}\frac{\partial \bar{T}}{\partial x} = -(\gamma - 1)\frac{\bar{u}^2}{\bar{a}^2}\frac{\partial \bar{u}}{\partial x}, \tag{4.5}$$

can be used to develop the model (4.3) further. Here, $\bar{a}$ is the mean speed of sound. We obtain

$$\bar{u}\frac{\partial \epsilon_s}{\partial x} = -[c_\omega(1 + b'_\omega A_{uT}) - 1 + \alpha(\gamma - 1)M^2]\epsilon_s \frac{\partial \bar{u}}{\partial x} = -\frac{2}{3}c_{\epsilon 1}\epsilon_s \frac{\partial \bar{u}}{\partial x}, \tag{4.6}$$

where $c_{\epsilon 1} = (3/2)[c_\omega(1 + b'_\omega A_{uT}) - 1 + \alpha(\gamma - 1)M^2]$ is a function of the local Mach number, and a factor of $2/3$ is included in (4.6) to match the form of standard $k - \epsilon$ equations. For cases where upstream Mach number is known, a more convenient form of $c_{\epsilon 1}$ can be derived by expressing the temperature ratio in terms of the velocity ratio across the shock. It can be easily checked that

$$\frac{\bar{T}_2}{\bar{T}_1} = \left(\frac{\bar{u}_1}{\bar{u}_2}\right)^{aM_1+b}, \tag{4.7}$$

where $a = 0.185$ and $b = 0.175$ give a close approximation to the exact value. Thus,

$$c_{\epsilon 1} = \tfrac{3}{2}[c_\omega(1 + b'_\omega A_{uT}) - 1 + \alpha(aM_1 + b)]. \tag{4.8}$$

Substituting the values of different parameters gives the following form of the final model constant:

$$c_{\epsilon 1} \simeq 1 + 0.21M_1 + 0.3A_{uT}(1 + \mathrm{e}^{1-M_1}), \tag{4.9}$$

which yields practically identical results to the model equation (4.3), as can be seen in figure 7. The final modelled form of the ϵ_s-equation can therefore be written in a frame-independent form as

$$\bar{\rho}\bar{u}_i\frac{\partial \epsilon_s}{\partial x_i} = -\frac{2}{3}c_{\epsilon 1}\bar{\rho}\epsilon_s\bar{s}_{jj} - c_{\epsilon 2}\frac{\bar{\rho}\epsilon_s^2}{k}, \tag{4.10}$$

where $\bar{s}_{jj} = \partial \bar{u}_j/\partial x_j$ is the mean dilatation. A viscous dissipation term similar to that used in the standard k–ϵ model (Wilcox 1998) is added, and the value of the model constant $c_{\epsilon 2}$ is set to reproduce the decay rate of homogeneous isotropic turbulence in the DNS.

Sinha *et al.* (2003) present an alternative equation for the model constant $c_{\epsilon 1}$ for purely vortical turbulence interacting with a shock wave. The values of the model constant are within 3 % of those obtained using (4.9), and make practically no difference to the DNS test cases with $A_{uT} \simeq 0$ described below. The equation was subsequently extended to non-zero A_{uT} cases by Veera & Sinha (2009). These earlier forms of $c_{\epsilon 1}$ are based purely on empirical curve-fitting to LIA data. By comparison, the current model is based on a rigorous equation for the evolution of the solenoidal dissipation rate across the shock derived from the Navier–Stokes equations. The physical mechanisms that contribute to the amplification of ϵ_s are systematically analysed to arrive at the final form of the model equation presented above.

4.2. *Model for turbulent kinetic energy*

The modelling of turbulent kinetic energy (TKE) amplification in the interaction of homogeneous turbulence with a normal shock is discussed in detail by Sinha *et al.* (2003) and Veera & Sinha (2009). The key results are presented below.

The TKE equation in the k–ϵ turbulence model (Wilcox 1998) applied to shock/homogeneous turbulence interaction is given as

$$\tilde{u}\,\frac{\partial k}{\partial x} = -\widetilde{u''^2}\frac{\partial \tilde{u}}{\partial x} - \epsilon_s, \tag{4.11}$$

where compressibility corrections in the form of dilatational dissipation and pressure–dilatation effects are neglected, as they are not found to improve predictions in shock/homogeneous turbulence interactions (Sinha *et al.* 2003). Using the Boussinesq approximation, the Reynolds stress $\widetilde{u''^2}$ is given by

$$\bar{\rho}\widetilde{u''^2} = -\frac{4}{3}\mu_T\frac{\partial\tilde{u}}{\partial x} + \frac{2}{3}\bar{\rho}k, \tag{4.12}$$

where the eddy viscosity $\mu_T = c_\mu\bar{\rho}k^2/\epsilon_s$ and $c_\mu = 0.09$. Substitution in (4.11) results in a production term that is proportional to $(\partial\tilde{u}/\partial x)^2$. The source term assumes large values ($\propto 1/\bar{\delta}^2$) at a shock wave, and this leads to high amplification of turbulent kinetic energy. Also, the amplification increases rapidly as the grid is refined to get a thinner shock. Sinha *et al.* (2003) argue that this non-physical behaviour of the standard k–ϵ model is primarily caused by the breakdown of the eddy-viscosity assumption in a highly non-equilibrium flow, such as a shock wave.

Algebraic Reynolds stress models are independent of the eddy-viscosity formulation, and therefore expected to perform better than the standard k–ϵ model. The equivalent nonlinear eddy-viscosity models suppress the model parameter c_μ in regions of high mean flow gradient. Suppressing eddy viscosity in the shock wave leads to a reduction in the k-amplification level, and brings it closer to the DNS data. A limiting case of the nonlinear eddy-viscosity models is to set $\mu_T = 0$ in the shock wave, and it yields the isotropic form of the Reynolds stress $\widetilde{u''^2} = 2k/3$. The resulting equation matches DNS amplification of TKE for Mach numbers lower than 1.4 (see figure 5 in Sinha *et al.* 2003).

Further, a model is proposed to include the damping effect of the unsteady shock motion, and it results in a good match with theory and DNS over the entire range of Mach numbers (Sinha *et al.* 2003). The presence of non-zero velocity–temperature correlation in the incoming flow is known to affect TKE amplification across the shock (Mahesh *et al.* 1997). The corresponding source term in the TKE equation is positive for negatively correlated velocity and temperature fluctuations ($A_{uT} > 0$) and has a damping effect for positive correlations ($A_{uT} < 0$). Veera & Sinha (2009) propose a physically consistent model for this effect. The final model form as applicable to the shock/homogeneous turbulence interactions considered in this section is given by

$$\bar{\rho}\bar{u}_i\frac{\partial k}{\partial x_i} = -\frac{2}{3}\bar{\rho}k\bar{s}_{jj}\left[1 - b_1' + \frac{A_{uT}}{2}\left(1 + \frac{1}{T_r}\right)\right] - \bar{\rho}\epsilon_s, \tag{4.13}$$

and is found to match theory and DNS data well. Here, $b_1' = b_{1,\infty}'(1 - \mathrm{e}^{1-M_1})$ is the shock-unsteadiness modelling parameter and $b_{1,\infty}' = 0.4 + 0.2A_{uT}$ is its high-Mach-number limiting value. The mean temperature ratio across the shock is given by $T_r = \overline{T}_2/\overline{T}_1$, and we use $\tilde{u} \simeq \bar{u}$ as noted in § 2. Further details can be found in the work of Veera & Sinha (2009).

4.3. *Comparison with DNS data*

The k–ϵ model developed above is compared with DNS data for shock/homogeneous turbulence interaction for a range of upstream conditions (see table 1). Other k–ϵ models commonly used in the literature are also presented. The first four cases bring out the effect of upstream entropy fluctuations on shock–turbulence interaction, and are studied first. Comparison with the high-Mach-number interactions of Larsson & Lele (2009) are presented subsequently.

Case	M_1	A_{uT}	M_t	Re_λ	k_{in}	ϵ_{in}	Source
1.29A	1.29	0.04	0.14	19.1	9.8×10^{-3}	1.3×10^{-3}	Mahesh *et al.* (1997)
1.29B	1.29	0.56	0.14	19.1	9.8×10^{-3}	1.3×10^{-3}	Mahesh *et al.* (1997)
1.5A	1.50	0.01	0.17	6.7	1.5×10^{-2}	4.2×10^{-3}	Jamme *et al.* (2002)
1.5B	1.50	0.82	0.17	6.7	1.5×10^{-2}	4.2×10^{-3}	Jamme *et al.* (2002)
2.5	2.50	0.00	0.22^a	40.0^a	2.7×10^{-2}	9.9×10^{-4}	Larsson & Lele (2009)
3.5	3.50	0.00	0.22^a	40.0^a	2.6×10^{-2}	9.7×10^{-4}	Larsson & Lele (2009)
4.7	4.70	0.00	0.22^a	40.0^a	2.6×10^{-2}	9.5×10^{-4}	Larsson & Lele (2009)

TABLE 1. Mean and turbulent flow quantities for the interaction of homogeneous turbulence with a normal shock. Values are reported either at the inflow station or immediately upstream of the shock (marked by ^{a}). The turbulence quantities k and ϵ are normalized by the upstream values of $\bar{\rho}$, $\bar{a}$ and $\bar{\mu}$.

4.3.1. *Effect of entropy fluctuations*

The cases 1.29A and 1.5A have essentially vortical inflow turbulence, and cases 1.29B and 1.5B have an entropic thermodynamic field along with vortical velocity fluctuations in the incoming flow. Morkovin's hypothesis holds in a weak form, such that u_{rms} and T_{rms} upstream of the shock wave follow (1.1):

$$\frac{\overline{u'T'}}{\bar{u}\bar{T}} = R_{u'T'}\frac{u_{rms}}{\bar{u}}\frac{T_{rms}}{\bar{T}} = (\gamma - 1)M_1^2 R_{u'T'}\frac{\overline{u'^2}}{\bar{u}^2}, \tag{4.14}$$

where the cross-correlation coefficient $R_{u'T'}$ is given for each case. The above equation is compared with (1.2) to obtain the equivalent A_{uT} for the cases listed in table 1. The values of Reynolds number based on the Taylor microscale, Re_λ, and turbulent Mach number, M_t, at the inflow station are also tabulated. These are used to compute the inlet values of k and ϵ_s at $x = 0$. Details are given in Veera & Sinha (2009), and are not repeated here.

The evolution of the streamwise and transverse vorticity variances obtained from the DNS are presented by Mahesh *et al.* (1997) and Jamme *et al.* (2002). These are used along with the kinematic viscosity of the fluid to compute the variation in solenoidal dissipation rate (see figure 8). The data show a monotonic decay of ϵ_s from its inflow level to a normalized value of unity immediately upstream of the shock. There is a sharp increase at the shock, which is located at $x = 2$ for Mach 1.29 cases and at $x = 3$ for the Mach 1.5 flows. This is followed by a further decay of ϵ_s downstream of the shock wave.

The model equations (4.10) and (4.13) are non-dimensionalized using the upstream values of $\bar{\rho}$, $\bar{a}$ and $\bar{\mu}$. The reference length scale, L, in cases 1.29A and 1.29B is chosen such that the Reynolds number based on the reference quantities, Re_L, is 750 (Mahesh *et al.* 1997). Cases 1.5A and 1.5B use a characteristic length of 2λ as reference, where λ is the Taylor microscale as defined by Tennekes & Lumley (1972). Note that a value of $c_{\epsilon 2} = 1.5$ is used in the modelled ϵ_s-equation to match the decay rate upstream of the shock wave.

The turbulence model equations are solved fully coupled with the conservation equations for mean flow. A finite-volume code based on a low-dissipation form of the Steger–Warming flux–vector splitting approach (MacCormack & Candler 1989) is used for this purpose. The viscous fluxes are discretized using a central-difference scheme, and an explicit time integration is used to reach a steady-state solution. The code has

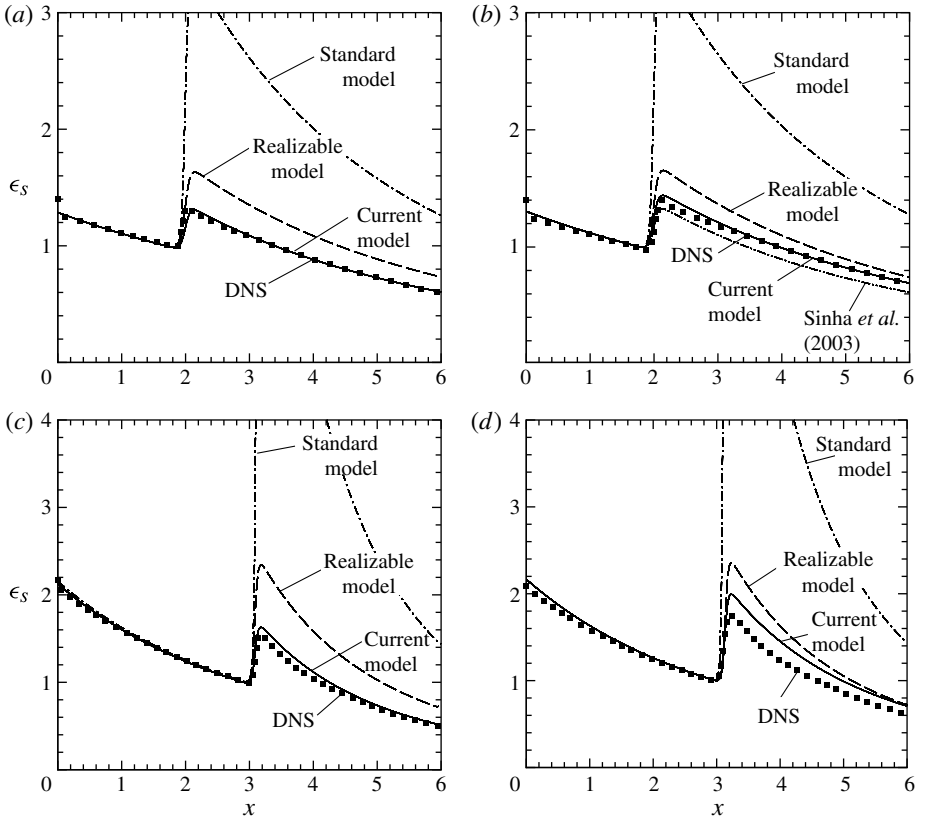

FIGURE 8. Evolution of solenoidal dissipation rate in homogeneous turbulence passing through a normal shock for cases (*a*) 1.29A, (*b*) 1.29B, (*c*) 1.5A and (*d*) 1.5B listed in table 1. Different versions of the k–ϵ model are compared with DNS data (Mahesh *et al.* 1997; Jamme *et al.* 2002).

been validated for several supersonic and hypersonic applications (Sinha, Mahesh & Candler 2005; Pasha & Sinha 2008, 2012). The mean flow variables are initialized to a hyperbolic tangent profile centred at the DNS shock location. The upstream and downstream boundary values are matched to the Rankine–Hugoniot conditions. The turbulent quantities k and ϵ_s are initialized to their inlet values listed in table 1. The results presented in figure 8 are computed on a mesh with 200 grid points distributed uniformly between the inlet (at $x = 0$) and the outlet (at $x = 6$). Sensitivity of the results to the grid resolution is described below.

As discussed earlier, the standard k–ϵ model predicts a high amplification of ϵ_s across the shock wave (see figure 8). For the 1.29A case, it predicts a peak ϵ_s value of 3.52 compared to that of 1.33 in the DNS. Suppressing eddy viscosity in the shock region by the realizable k–ϵ model (Thivet *et al.* 2001) brings down the post-shock ϵ_s level, but the values are still higher than DNS. The current model, on the other hand, predicts the amplification of ϵ_s across the shock as well as the downstream decay rate correctly. The presence of upstream temperature fluctuations (case 1.29B) enhances ϵ_s-amplification at the shock, and it is matched well by the current model. By comparison, the standard and realizable k–ϵ models are insensitive to the nature

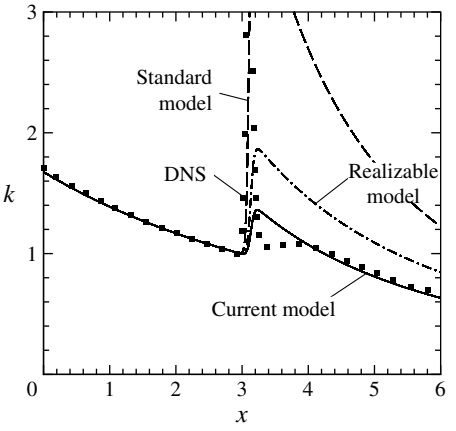

FIGURE 9. Evolution of turbulent kinetic energy k in the interaction of homogeneous turbulence with a normal shock for case 1.5A. Different versions of the k–ϵ model are compared with DNS data (Jamme *et al.* 2002).

of upstream turbulence, and their results are identical to the respective predictions in 1.29A. The k–ϵ model proposed by Sinha *et al.* (2003) is also independent of A_{uT}. Its predictions match the current model closely for the 1.29A flow, but are appreciably lower than DNS for 1.29B with non-zero A_{uT}.

A stronger shock wave at Mach 1.5 yields a higher amplification of ϵ_s across the shock compared to the Mach 1.29 flows. The standard and realizable k–ϵ models, once again, over-predict the post-shock ϵ_s value for 1.5A, and are insensitive to the presence of upstream temperature fluctuations in 1.5B. The current model results match DNS data well for solenoidal inflow turbulence (figure 8*c*) and over-predict the post-shock ϵ_s (by $\sim$15 % at the peak location) in the presence of entropy fluctuations in the upstream flow (figure 8*d*).

The evolution of turbulent kinetic energy predicted by the current model equations (4.10) and (4.13) is compared with DNS data for the case 1.5A in figure 9. Results computed using the standard and realizable k–ϵ models are also presented. The turbulent kinetic energy predicted by the current model matches DNS data well for solenoidal turbulence interacting with a normal shock at Mach 1.5. By comparison, the standard and realizable models lead to higher values of k downstream of the shock. The same is true for the other three test cases and the results are presented in Veera & Sinha (2009). Note that DNS yields a high level of turbulent kinetic energy in the region of the shock wave. This is caused by the unsteady shock motion and does not represent turbulent fluctuations. Also, the non-monotonic variation in k immediately downstream of the shock wave ($3.2 < x < 3.9$) is due to a rapid decay of acoustic energy in this region (Mahesh *et al.* 1997). This transfer between the acoustic and vortical modes is not explicitly reproduced, but its net effect on turbulent kinetic energy amplification is included in the current model. As a result, there is a close match between the model predictions and DNS data for $x > 3.9$.

4.3.2. *High-Mach-number interactions*

Application of the current model to the high-Mach-number cases of Larsson & Lele (2009) is presented next. The M_t and Re_λ values listed for these cases in table 1 are immediately upstream of the shock wave. They are extrapolated to the inlet

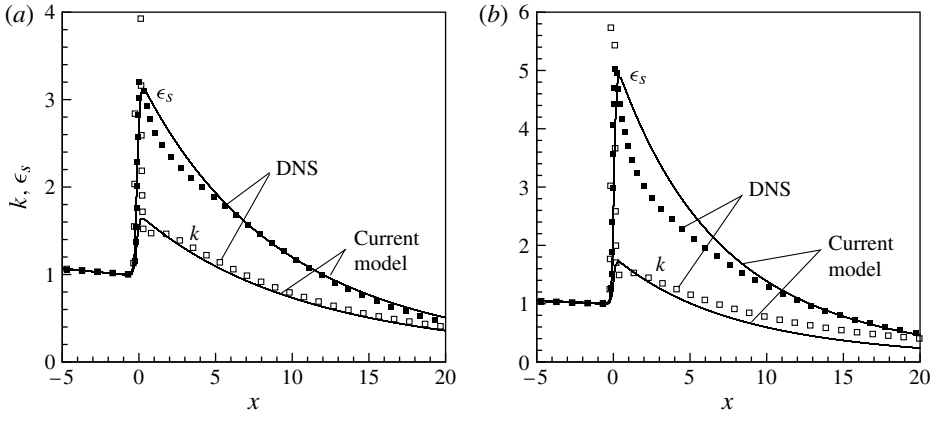

FIGURE 10. Model predictions (lines) for turbulent kinetic energy and solenoidal dissipation rate in the shock/homogeneous turbulence interaction cases (*a*) $M_1 = 2.5$ and (*b*) $M_1 = 3.5$ compared to DNS data (symbols) of Larsson & Lele (2009).

location using one-dimensional k–ϵ equations for decaying homogeneous isotropic turbulence. A value of $c_{\epsilon 2} = 1.2$ is used here. At a shock wave, the k–ϵ model equations in a RANS code can yield results that are significantly higher than those presented in figure 7 for the limiting inviscid case. The error is more prominent at high Mach numbers with relatively large turbulence amplification across the shock wave, and is due to the non-conservative nature of the k–ϵ source terms. The model equations (4.10) and (4.13) are therefore cast in an equivalent conservative form and the results are comparable to those obtained by direct integration of the inviscid equations (4.3). The values are slightly lower than those in figure 7 because of the effect of viscous dissipation in the shock region.

For the Mach 2.5 case, the current model predicts an ϵ_s-amplification of 3.12 at the shock wave and it is close to the peak value obtained in the DNS (see figure 10*a*). Downstream of the shock, the ϵ_s-decay rate is higher in the DNS, resulting in a mis-match with the model results for $0 < x < 6$. As noted by Larsson & Lele (2009), anisotropy in the Reynolds stresses and vorticity variances is prominent up to about $x = 10$. Further downstream, the model reproduces the value of ϵ_s and its decay rate closely. The turbulent kinetic energy comparison for this case is similar to that presented in figure 9. The model matches the k-amplification obtained from DNS, but is somewhat lower than the data downstream of the shock wave. This is probably due to the over-prediction of ϵ_s in the post-shock region. Further downstream ($x > 6$), the model results closely match the decay rate of turbulent kinetic energy in the DNS.

The model predictions for the Mach 3.5 case (in figure 10*b*) show a similar comparison with DNS. The amplification of k and ϵ_s at the shock is reproduced closely. Downstream of the shock, there is discrepancy between the data and prediction of the solenoidal dissipation rate in the near field. However, the model matches DNS data further downstream ($x > 10$). The far-field decay rate of the turbulent kinetic energy is comparable to that obtained from DNS, but the values are under-predicted by the model. The highest Mach number case 4.7 (not shown here) follows a similar trend. The near-field discrepancy between model and DNS is higher than the previous cases, but the turbulence amplification at the shock is predicted correctly.

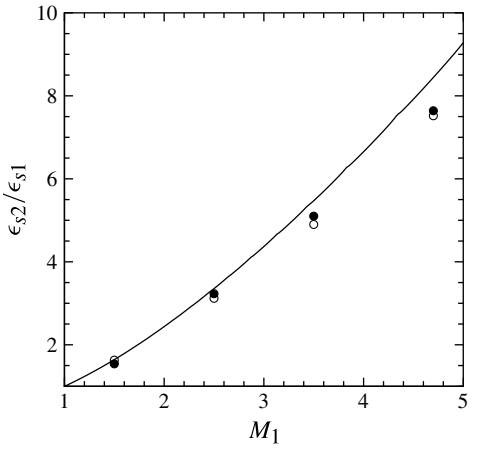

FIGURE 11. Comparison of ϵ_s-amplification across the shock obtained from linear theory (line), DNS (•) and RANS computations using the current k–ϵ model (○).

Figure 11 presents the amplification of ϵ_s obtained from the RANS simulations as a function of the upstream mean flow Mach number. The cases correspond to 1.5A, 2.5, 3.5 and 4.7, and the peak value of ϵ_s in the DNS are plotted. Linear analysis results for $A_{uT} = 0$ are also included for comparison. The RANS results are comparable to the linear theory at low Mach numbers, but are relatively lower for the hig-Mach-number cases. This may be due to the effect of viscous dissipation in the region of the shock wave, which is not accounted for by the inviscid linear theory. A higher dissipation rate for cases 3.5 and 4.7 results in a larger discrepancy between the RANS computation and linear theory. On the other hand, the DNS include viscous effects at the shock wave, and the corresponding ϵ_s-amplification values overlap with the RANS results.

Note that the current model based on linear theory reproduces the DNS data for turbulent kinetic energy, enstrophy and solenoidal dissipation rate fairly well. This is probably due to the fact that $M_t^2 \ll (M_1^2 - 1)$ for all the cases considered here. This condition is proposed by Lee *et al.* (1993) for the validity of LIA. There are, however, other aspects of shock–turbulence interaction that are not captured by the linear theory. For example, the streamwise vorticity variance shows a rapid build-up downstream of the shock to match the transverse vorticity components. The linearized governing equations, without the nonlinear terms, do not predict this increase in the streamwise vorticity. Additional modelling to account for the nonlinear effects may improve the model predictions further in the post-shock region. Also, Larsson & Lele (2009) note that incoming turbulence with $M_t^2 > 0.06(M_1^2 - 1)$ can result in significantly deformed or broken shock waves. Such strong interactions are clearly outside the scope of the current linearized analysis.

4.3.3. *Grid refinement study*

Sensitivity of the results presented above to the computational mesh is studied by varying the grid-point density at the shock. Case 1.5B is considered for the grid refinement study and the results are presented in figure 12. The baseline grid with 200 points, a finer mesh with 400 points and a coarser mesh with 100 points are used in the simulations. All the grids have uniformly spaced grid points throughout

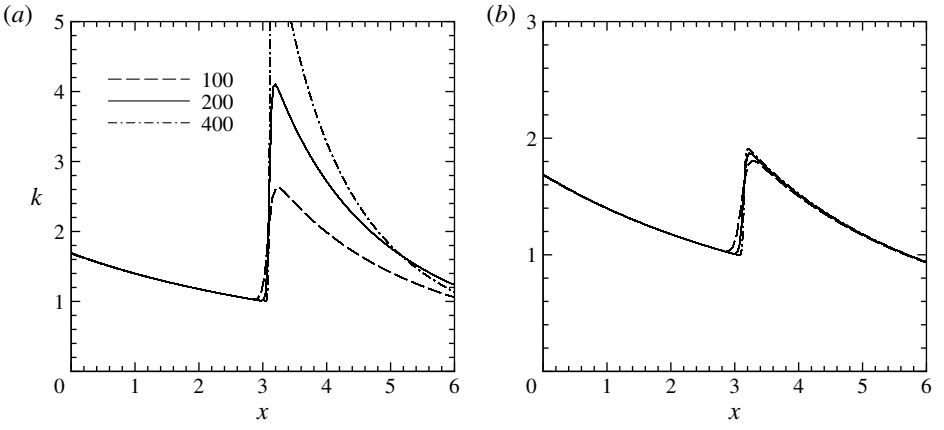

FIGURE 12. Amplification of turbulent kinetic energy in the shock/homogeneous turbulence interaction case 1.5B computed using varying numbers of grid points: (*a*) standard k–ϵ model; and (*b*) current k–ϵ model.

the computational domain, resulting in a cell size of 0.015, 0.03 and 0.06 for the fine, baseline and coarse meshes respectively.

As noted earlier, the standard k–ϵ model predictions (figure 12*a*) are highly sensitive to the computed shock thickness. The shock gets thinner with successive refinement of the computational mesh, and the k-amplification obtained using the standard model increases rapidly. The post-shock dissipation rate also increases with grid refinement, which results in a faster downstream decay of the turbulent kinetic energy computed on the finer mesh.

By comparison, predictions of the current and realizable k–ϵ models are fairly insensitive to the changes in computational mesh (see figure 12*b*). The variations are mostly localized in the region of the shock wave, and the post-shock turbulent kinetic energy shows a converging trend with successive grid refinement. The difference in peak values between the baseline and fine meshes is less than 2 %. The corresponding variation for the higher Mach number cases is less than 3 %. The trends in solenoidal dissipation rate, not shown here, are similar to that presented in the figure, with post-shock peak values predicted by the current model within 3.5 % between the two finer meshes.

5. Application to shock–boundary layer interactions

Interaction of turbulent boundary layers with shock waves forms an important class of problems for testing new turbulence models for high-speed flows. Several turbulence models and their modifications have been proposed for SBLI flows (Roy & Blottner 2006). We evaluate the potential of the current model in a canonical shock–boundary layer configuration.

In the current framework, the amplification of turbulent fluctuations at a shock wave depends on two parameters, namely the local strength of the shock wave given in terms of the shock-normal Mach number and the upstream velocity–temperature correlation. The mean flow Mach number and the local shock inclination angle can be obtained from a RANS solution. The shock-normal Mach number and its variation across the boundary layer can thus be computed; see previous work by Sinha *et al.*

(2005) and Pasha & Sinha (2008, 2012). On the other hand, the level of temperature fluctuations in a boundary layer and its correlation with the velocity fluctuations is not readily available in a RANS computation. Recent DNS studies of supersonic turbulent boundary layers shed light on this point.

Guarini *et al.* (2000) present DNS of a Mach 2.5 turbulent boundary layer at a Reynolds number based on momentum thickness of 1577. Morkovin's hypothesis (see § 1) and the strong Reynolds analogy relating velocity and temperature fluctuations in the flow are critically evaluated using the DNS data. They find that the relation between temperature and velocity fluctuations given in (1.1) is valid in a weak form up to $y/\delta_{BL} \simeq 0.6$. The temperature fluctuations are, however, higher than (1.1) estimate in the outer part of the boundary layer. A modified form of the strong Reynolds analogy (SRA) presented by Huang, Coleman & Bradshaw (1995),

$$\frac{T_{rms}}{\bar{T}} = (\gamma - 1)M_1^2 \frac{u_{rms}}{\bar{u}} \frac{1}{Pr_T} \left(1 - \frac{\partial \bar{T}_t}{\partial \bar{T}}\right)^{-1}, \tag{5.1}$$

is found to scale the fluctuations near the boundary layer edge better. Here, T_t is the total temperature, Pr_T is the turbulent Prandtl number and δ_{BL} is the boundary layer thickness.

Further, the streamwise velocity and temperature fluctuations are found to be anti-correlated with the correlation coefficient $R_{u'T'} \simeq -0.6$ for $0.2 < y/\delta_{BL} < 0.8$. It attains higher magnitude ($R_{u'T'} \sim -0.8$) in the near-wall region and falls off to negligible values at the boundary layer edge. Pirozzoli, Grasso & Gatski (2004) report similar trends for the correlation coefficient and SRA relations in a spatially evolving turbulent boundary layer at Mach 2.25. The modelling parameter A_{uT} is thus evaluated as

$$A_{uT} = -(\gamma - 1)M^2 \frac{R_{u'T'}}{Pr_T} \left(1 - \frac{\partial \bar{T}_t}{\partial \bar{T}}\right)^{-1} \tag{5.2}$$

and is applied to a Mach 2.25 turbulent boundary layer at conditions comparable to those of Pirozzoli *et al.* (2004). The parameter A_{uT} is found to follow the variation of M^2 across the boundary layer. It is close to zero in the low-Mach-number near-wall region. A maximum value of $A_{uT} \simeq 1.0$ is attained at $y/\delta_{BL} = 0.8$ before dropping to negligible values at the boundary layer edge. Upstream temperature fluctuations with $A_{uT} \sim 1$ can result in an enhancement of 30–40 % in the ϵ_s-amplification at the shock wave. Note that the variation in M and the derivative $\partial \bar{T}_t/\partial \bar{T}$ across the boundary layer are obtained from a RANS simulation. The turbulent Prandtl number is assumed to be 0.9.

Application of the current shock–turbulence model to practical SBLI configurations requires evaluation of A_{uT} in the upstream boundary layer. Models proposed for turbulent heat flux or energy flux can be used for this purpose. For example, Bowersox (2009) presents the following algebraic model for the streamwise energy flux in a zero-pressure-gradient boundary layer:

$$\overline{\rho e'' u''} = \tau_{12} \frac{\partial \tilde{h}}{\partial y} \tau_\theta - \tau_{22} \frac{\partial \tilde{h}}{\partial y} \frac{\partial \tilde{u}}{\partial y} \tau_\theta^2, \tag{5.3}$$

where e and h are the internal energy and enthalpy respectively, τ_{12} and τ_{22} are the shear and normal Reynolds stresses, $\tau_\theta = \sigma_\theta k/\epsilon$ is a turbulent time scale, and σ_θ is a model constant. The above equation can be readily rearranged to get an equivalent relation for A_{uT}, where all the quantities on the right-hand side can be obtained from

a RANS simulation. Note that a component normal to the shock wave is considered by modifying the value obtained from the above equation with respect to the shock inclination angle.

The SBLI test case considered here is a 24° compression corner at Mach 2.84 and Reynolds number per unit length of 6.8×10^7 m^{-1}. An experimental investigation of this nominally two-dimensional configuration is reported by Settles & Dodson (1994). Surface pressure and skin friction coefficient measured in the experiments are used for evaluating numerical solutions, for example, in an earlier work by Sinha *et al.* (2005). The simulation methodology followed here is identical to the previous study and is not repeated. The computational grid is also based on a detailed grid-refinement study reported by Sinha *et al.* (2005), and inlet conditions are specified to match the incoming turbulent boundary layer momentum thickness.

Simulations using the standard k–ϵ and k–ω turbulence models predict a delayed separation at the compression corner (Sinha *et al.* 2005). This is argued to be due to turbulence over-amplification at the shock wave. The shock-unsteadiness damping effect (Sinha *et al.* 2003) is incorporated to reduce the amplification of turbulent kinetic energy. The separation location thus moves upstream, and the modified turbulence model predictions match the experimental measurements better. The Spalart–Allmaras (SA) model exhibits an opposite trend compared to the two-equation turbulence models. The standard SA model predicts an early separation, and applying the shock-unsteadiness correction moves the separation point downstream.

The standard SA model solves a transport equation for $\bar{\rho}\tilde{\nu}$, where $\tilde{\nu}$ is related to the turbulent kinematic viscosity ν_T via a wall damping function. In the transport equation, the turbulence production due to mean flow gradients is a function of the mean vorticity. The strong dilatation in a shock wave has only a small effect (less than 5 % in this case) on the turbulent kinematic viscosity. Noting that $\nu_T \propto k^2/\epsilon_s$ in the absence of appreciable dilatational dissipation in a boundary layer, the changes in ν_T across the shock can be estimated in terms of the amplifications of k and ϵ_s. The model equations (4.10) and (4.13) are thus used to propose an additional source term of the form $-c'_{b1}\bar{\rho}\tilde{\nu}S_{ii}$ in the transport equation for $\bar{\rho}\tilde{\nu}$. Here, the coefficient

$$c'_{b1} = \frac{4}{3}\left[1 - b'_1 + \frac{1}{2}A_{uT}\left(1 + \frac{1}{T_r}\right)\right] - \frac{2}{3}c_{\epsilon 1}, \tag{5.4}$$

and the parameters b'_1 and $c_{\epsilon 1}$ have been reported earlier. The additional source term is effective only in regions of strong compression and does not alter the standard SA model elsewhere in a flow. A similar correction to the SA model was proposed by Sinha *et al.* (2005), but the effect of upstream entropy fluctuations via A_{uT} was not included.

The variation of A_{uT} in the undisturbed turbulent boundary layer upstream of the compression corner is plotted in figure 13(*a*). The distribution of the upstream shock-normal Mach number along the separation shock is also shown. The model coefficient c'_{b1} computed using these values of M_{1n} and A_{uT} (see figure 13*b*) varies from near zero close to the wall to a maximum of 1.2 at $y/\delta_0 = 0.73$. Positive values of c'_{b1} lead to an amplification of ν_T across the shock, thus delaying flow separation. This results in an improved match with the experimental results.

The normalized surface pressure and skin friction coefficient measured in the experiment are compared with the computed solution in figure 14. The streamwise distance s along the plate and the ramp is normalized by the incoming boundary layer thickness δ_0, where $s = 0$ represents the corner. The experimental pressure rise

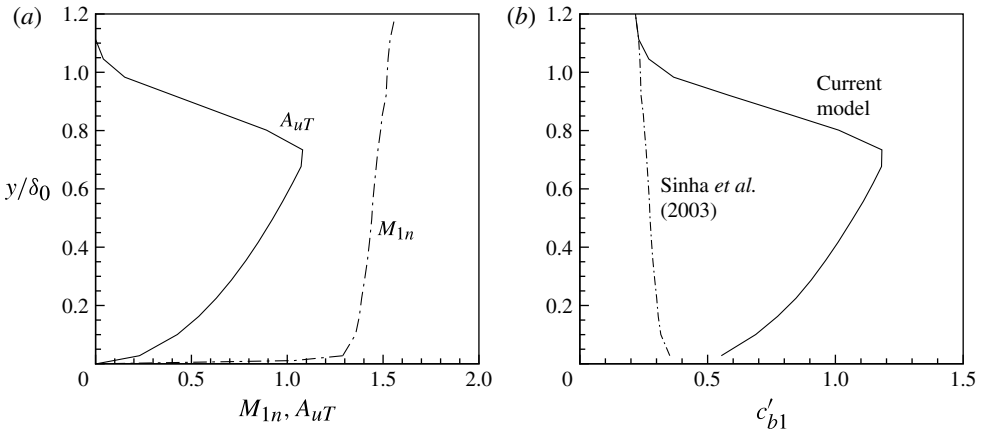

FIGURE 13. Variation of model parameters A_{uT}, M_{1n} and c'_{b1} in a 24° compression ramp SBLI flow. The wall-normal distance y is normalized by the undisturbed boundary layer thickness δ_0 upstream of the interaction.

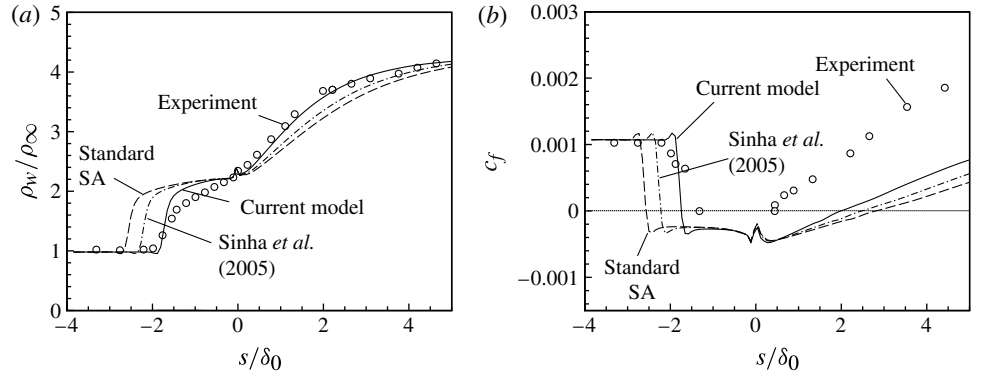

FIGURE 14. Comparison of (*a*) normalized surface pressure and (*b*) skin friction coefficient along a 24° compression corner obtained using different versions of the SA model with experimental data of Settles & Dodson (1994).

(at $s/\delta_0 = -2$) corresponds to the separation shock location, and it is reproduced well by the current model. The pressure plateau in the recirculation region is slightly over-predicted, but the reattachment pressure rise for $s > 0$ is closely matched by the simulation. The standard SA model, on the other hand, predicts the separation shock pressure rise far upstream of the experiment and the surface pressure in the reattachment region is under-predicted. The drop in skin friction coefficient from its flat-plate value marks the onset of separation, and it is also reproduced well by the current model. However, the separation bubble size, as indicated by the $c_f = 0$ data points, is over-predicted by both standard and modified SA models. Also, the computed skin friction coefficient on the ramp is much lower than the experimental measurement, and the current modification improves it by a small amount.

The results obtained using the shock-unsteadiness model (Sinha *et al.* 2005) are presented for comparison. The value of c'_{b1} across the boundary layer for this case

(obtained using $A_{uT} = 0$, see figure 13*b*) is significantly lower than the current model, and it results in a lower amplification of the turbulent eddy viscosity across the shock wave. The shock-unsteadiness modification thus shows only a moderate improvement in predicting the separation shock location (see figure 14), and is not enough to match the experimental data. It is essential to include the effect of upstream temperature fluctuations in the incoming boundary layer to match the onset of shock-induced flow separation in this flow.

The implementation of the current shock–turbulence modification in two-equation turbulence models can follow a procedure similar to that outlined in Sinha *et al.* (2005). The turbulence production term in the original models is suppressed in the shock wave and the model coefficients are matched to those in (4.10) and (4.13). This requires identifying high-compression regions of the flow field and is achieved by using an empirical function f_s. The standard model is thus recovered in regions outside the shock wave. By comparison, the mean-dilatation based correction for the SA model is effective only in the shock wave and does not require the additional variability due to the shock-identifying function to retain the standard form of the model elsewhere.

Wilcox (2008) presents a k–ω stress-limiter turbulence model that limits TKE production in a shock wave. It reduces the error caused by the eddy-viscosity assumption and thus improves SBLI predictions compared to the standard k–ω model; see, for example, figure 17 in Wilcox (2008). Further, Reynolds stress models are independent of the eddy-viscosity assumption, and are therefore expected to include the anisotropy effects at a shock wave. The shock–turbulence correction, presented in this work, should consequently be smaller in magnitude when such turbulence models are applied to SBLI flows. The models, however, may require additional development to account for the effect of upstream temperature fluctuations.

The results presented above show the potential of the current model in a supersonic compression ramp SBLI flow. Other configurations like two-dimensional oblique shock impingement, axisymmetric cone–flare and cylinder–flare, and three-dimensional single and double fins can also be used for model validation. In addition to the geometry, these test cases vary in terms of Mach number, Reynolds number and shock angle. Application of the shock–turbulence modification, like the model proposed by Sinha *et al.* (2003), show that the majority of the effect is localized at the separation shock. The separation location is better predicted by the modification, and this results in an improved flow topology and shock structure (Pasha & Sinha 2008, 2012).

The model coefficients in (4.10) and (4.13) are a function of the local shock strength, and the velocity–temperature correlation in the incoming flow. The results can therefore be sensitive to the free stream and boundary conditions. The parameter A_{uT} scales with the square of the upstream Mach number, and can have a large effect in hypersonic flows. The temperature boundary condition can further alter the value of A_{uT} in the vicinity of the wall. A detailed validation of the current model against different canonical configurations at varying Mach numbers, for both adiabatic and isothermal walls, is a subject of further investigation.

6. Conclusions

This paper studies the amplification of enstrophy when homogeneous isotropic turbulence interacts with a normal shock. Upstream turbulence with varying levels of vortical and entropic fluctuations are considered for a range of shock strengths. A linearized transport equation is derived for the evolution of enstrophy in the immediate

vicinity of the shock wave. The equation is written in a frame of reference attached to the unsteady shock wave, and assumes a separation of scales between the shock gradient and turbulent fluctuations. An integrated form of the equation is used to compute a budget of the enstrophy jump across the shock. It is found that mean compression at the shock plays a dominant role in amplifying enstrophy, and the baroclinic torque due to mean pressure gradient has an appreciable effect for non-zero temperature fluctuations in the upstream flow. The baroclinic source term is positive for negatively correlated temperature and velocity fluctuations upstream of the shock, and vice-versa.

The baroclinic term in the enstrophy equation is proportional to the correlation of transverse vorticity and density fluctuation gradient. A closure approximation is proposed for this correlation based on linear analysis results. This, along with a model for the production term, yields a closed-form solution for the enstrophy jump across a shock wave in the inviscid limit. The results are found to match enstrophy amplifications obtained from LIA for a range of shock strengths and varying ratio of upstream vortical to entropic fluctuations. The enstrophy equation is then used to develop a model for the solenoidal dissipation rate, and the resulting k–ϵ equations are employed to simulate the interaction of homogeneous isotropic turbulence with normal shock waves. The model predictions match the amplification of solenoidal dissipation rate in the DNS closely. There are however appreciable differences in the post-shock evolution of turbulence, possibly due to nonlinear effects not included in the current model. The model equations are further used to propose a modification to the eddy-viscosity transport equation in the SA turbulence model. Application to a canonical shock–boundary layer interaction shows that including the baroclinic effects on enstrophy generation at the shock results in a significantly closer match with experimental measurements.

Acknowledgements

The author wishes to acknowledge the contribution of V. K. Veera, a graduate student under the supervision of the author, for the preliminary development of the equations presented in this article. The author is grateful to Dr Johan Larsson of the Center for Turbulence Research, Stanford University, for his active help in analysing their DNS data. The author would also like to thank Dr S. Jamme of Institut Superieur de l'Aeronautique et de l'Espace (ISAE) for providing DNS data for model evaluation.

Appendix

This Appendix presents the scaling of the different terms in the enstrophy equation at the shock wave. The vorticity transport equation in a compressible flow is given by

$$\frac{\partial \omega_i}{\partial t} + u_j \frac{\partial \omega_i}{\partial x_j} = \omega_j \frac{\partial u_i}{\partial x_j} - \omega_i \frac{\partial u_j}{\partial x_j} + \nu \frac{\partial^2 \omega_i}{\partial x_j^2} - (\nabla \rho^{-1} \times \nabla p)_i + \psi_i, \tag{A 1}$$

where the terms on the left-hand side represent unsteady and convection effects. The first term on the right-hand side corresponds to vortex stretching and tilting, and the second term brings in the effect of non-zero dilatation in a compressible flow. The third term is viscous diffusion and the fourth term represents baroclinic torques. The last term brings in additional effects due to variation in fluid viscosity and is given by

$$\psi_i = \epsilon_{ijk} \frac{\partial \nu}{\partial x_j} \frac{\partial^2 u_k}{\partial x_l^2} + \frac{\epsilon_{ijk}}{3} \frac{\partial \nu}{\partial x_j} \frac{\partial^2 u_l}{\partial x_k \partial x_l} + \epsilon_{ijk} \frac{\partial}{\partial x_j} \left[\frac{1}{\rho} \frac{\partial \mu}{\partial x_l} \left(\frac{\partial u_k}{\partial x_l} \frac{\partial u_l}{\partial x_k} \right) - \frac{2}{3\rho} \frac{\partial \mu}{\partial x_k} \frac{\partial u_l}{\partial x_l} \right], \tag{A 2}$$

where ν is the kinematic viscosity of the fluid and ϵ_{ijk} is the third-order alternating tensor.

In the current problem with one-dimensional mean flow and zero mean vorticity, (A 1) can be written for the fluctuating vorticity components ω_i'. For the transverse vorticity fluctuations ω_z', we have

$$\begin{aligned}\frac{\partial \omega_z'}{\partial t} + (\bar{u} + u')\frac{\partial \omega_z'}{\partial x} + v'\frac{\partial \omega_z'}{\partial y} + w'\frac{\partial \omega_z'}{\partial z} = {} & \omega_x'\frac{\partial w'}{\partial x} + \omega_y'\frac{\partial w'}{\partial y} + \omega_z'\frac{\partial w'}{\partial z} \\ & - \omega_z'\left(\frac{\partial \bar{u}}{\partial x} + \frac{\partial u'}{\partial x} + \frac{\partial v'}{\partial y} + \frac{\partial w'}{\partial z}\right) \\ & + \bar{\nu}\left(\frac{\partial^2 \omega_z'}{\partial x^2} + \frac{\partial^2 \omega_z'}{\partial y^2} + \frac{\partial^2 \omega_z'}{\partial z^2}\right) \\ & + \frac{1}{\bar{\rho}^2}\frac{\partial \bar{\rho}}{\partial x}\frac{\partial p'}{\partial y} - \frac{1}{\bar{\rho}^2}\frac{\partial \bar{p}}{\partial x}\frac{\partial \rho'}{\partial y}\end{aligned} \tag{A 3}$$

where the baroclinic terms that are nonlinear in fluctuating pressure and density are neglected. Also, the ψ_3 term representing the effects of gradients and fluctuations in fluid viscosity has been dropped. These are assumed to be small compared to the diffusion due to mean viscosity that is included in the equation.

The scaling of the different terms is given below. The temporal variations in ω_z' at a fixed point caused by the turbulent fluctuations scale with the turbulent time scale $\hat{u}/\ell$, and are smaller than those due to the unsteady shock passing through the point. The unsteady shock motion is caused by the incoming turbulent fluctuations, and therefore the instantaneous shock speed ξ_t is taken to be of order $\hat{u}$ in magnitude. This along with the instantaneous shock thickness δ gives the following estimate for the time rate of change in vorticity at the shock wave:

$$\frac{\partial \omega_z'}{\partial t} \sim \frac{\xi_t}{\delta}\frac{\hat{u}}{\ell} \sim \frac{\hat{u}^2}{\delta \ell}, \tag{A 4}$$

where ω_z' is assumed to be of order $\hat{u}/\ell$ in magnitude. The convection due to mean and fluctuating velocities scales as

$$\bar{u}\frac{\partial \omega_z'}{\partial x} \sim \frac{\hat{u}U}{\delta \ell}, \quad u'\frac{\partial \omega_z'}{\partial x} \sim \frac{\hat{u}^2}{\delta \ell} \quad \text{and} \quad v'\frac{\partial \omega_z'}{\partial y} \sim w'\frac{\partial \omega_z'}{\partial z} \sim \frac{\hat{u}^2}{\ell^2}. \tag{A 5}$$

The vortex stretching/tilting terms for ω_z' do not have a contribution from the mean velocity gradient, and therefore are relatively small in magnitude.

$$\omega_x'\frac{\partial w'}{\partial x} \sim \frac{\hat{u}^2}{\delta \ell} \quad \text{and} \quad \omega_y'\frac{\partial w'}{\partial y} \sim \omega_z'\frac{\partial w'}{\partial z} \sim \frac{\hat{u}^2}{\ell^2}. \tag{A 6}$$

The effect of mean and fluctuating dilatation on the transverse vorticity fluctuations scales as

$$\omega_z'\frac{\partial \bar{u}}{\partial x} \sim \frac{\hat{u}U}{\delta \ell}, \quad \omega_z'\frac{\partial u'}{\partial x} \sim \frac{\hat{u}^2}{\delta \ell} \quad \text{and} \quad \omega_z'\frac{\partial v'}{\partial y} \sim \omega_z'\frac{\partial w'}{\partial z} \sim \frac{\hat{u}^2}{\ell^2}. \tag{A 7}$$

The baroclinic torque due to the mean pressure gradient is estimated as

$$\frac{1}{\bar{\rho}^2}\frac{\partial \rho'}{\partial y}\frac{\partial \bar{p}}{\partial x} \sim \frac{1}{\bar{\rho}_1^2}\frac{\bar{\rho}_1}{\ell}\frac{\hat{u}}{U}\frac{\bar{\rho}_1 U^2}{\delta} \sim \frac{\hat{u}U}{\delta \ell}, \tag{A 8}$$

where $\bar{\rho}_1$ is the characteristic mean density. The normalized density fluctuations are assumed to be comparable to the normalized velocity fluctuations, i.e. $\rho'/\bar{\rho}_1 \sim \hat{u}/U$, and the mean pressure scales as $\bar{\rho}_1 U^2$. The second baroclinic term due to mean density gradient, on the other hand, scales as

$$\frac{1}{\bar{\rho}^2}\frac{\partial \bar{\rho}}{\partial x}\frac{\partial p'}{\partial y} \sim \frac{U^2}{\delta}\frac{p'}{\bar{p}_1}. \tag{A 9}$$

Noting that the pressure fluctuations are small compared to the density fluctuations in the test flows considered in this work, we have

$$\frac{1}{\bar{\rho}^2}\frac{\partial \bar{\rho}}{\partial x}\frac{\partial p'}{\partial y} \ll \frac{U^2}{\delta}\frac{\rho'}{\bar{\rho}_1} \sim \frac{\hat{u}U}{\delta \ell}. \tag{A 10}$$

The viscous diffusion terms scale as

$$\bar{\nu}\frac{\partial^2 \omega_z'}{\partial x^2} \sim \frac{\bar{\nu}_1}{\delta^2}\frac{\hat{u}}{\ell} \quad \text{and} \quad \bar{\nu}\frac{\partial^2 \omega_z'}{\partial y^2} \sim \bar{\nu}\frac{\partial^2 \omega_z'}{\partial z^2} \sim \frac{\bar{\nu}_1}{\ell^2}\frac{\hat{u}}{\ell}, \tag{A 11}$$

where $\bar{\nu}_1$ is the characteristic mean kinematic viscosity of the fluid. It can be easily seen that the ratio of the leading inertial terms in (A 5) to the largest viscous term is $U\delta/\bar{\nu}_1$, which is assumed to be of order unity in § 2. Thus, the dominant terms in (A 2) are

$$\bar{u}\frac{\partial \omega_z'}{\partial x} + \omega_z'\frac{\partial \bar{u}}{\partial x} - \frac{1}{\bar{\rho}^2}\frac{\partial \bar{\rho}}{\partial x}\frac{\partial p'}{\partial y} + \frac{1}{\bar{\rho}^2}\frac{\partial \bar{p}}{\partial x}\frac{\partial \rho'}{\partial y} - \bar{\nu}\frac{\partial^2 \omega_z'}{\partial x^2} = 0 \tag{A 12}$$

where the baroclinic term due to the mean density gradient is retained for the sake of generality. Taking a moment with ω_z' and Reynolds averaging yields the following equation for $\overline{\omega_z'^2}$:

$$\bar{u}\frac{\partial}{\partial x}\left(\frac{\overline{\omega_z'^2}}{2}\right) = -\overline{\omega_z'^2}\frac{\partial \bar{u}}{\partial x} - \overline{\omega_z' \rho'_{,y}}\frac{1}{\bar{\rho}^2}\frac{\partial \bar{p}}{\partial x} + \overline{\omega_z' p'_{,y}}\frac{1}{\bar{\rho}^2}\frac{\partial \bar{\rho}}{\partial x} + \bar{\nu}\frac{\partial^2}{\partial x^2}\left(\frac{\overline{\omega_z'^2}}{2}\right) - \bar{\nu}\overline{\frac{\partial \omega_z'}{\partial x}\frac{\partial \omega_z'}{\partial x}}, \tag{A 13}$$

where the last two terms correspond to viscous diffusion and dissipation. The scaling of these terms is similar to those in the instantaneous equation, except for a change in the characteristic length in the shock-normal direction. The variation across the time-averaged shock wave is taken over a length scale $\bar{\delta}$ (see figure 1), which is the mean shock thickness obtained by averaging across a fluctuating shock wave.

The magnitudes of the convection and viscous terms in (A 13) are thus

$$\bar{u}\frac{\partial}{\partial x}\left(\frac{\overline{\omega_z'^2}}{2}\right) \sim \frac{U}{\bar{\delta}}\frac{\hat{u}^2}{\ell^2}, \tag{A 14}$$

$$\bar{\nu}\frac{\partial^2}{\partial x^2}\left(\frac{\overline{\omega_z'^2}}{2}\right) \sim \bar{\nu}\overline{\frac{\partial \omega_z'}{\partial x}\frac{\partial \omega_z'}{\partial x}} \sim \frac{\bar{\nu}_1}{\bar{\delta}^2}\frac{\hat{u}^2}{\ell^2}, \tag{A 15}$$

and the ratio of the inertial to viscous effects scales as

$$\frac{U\bar{\delta}}{\bar{\nu}_1} \sim \frac{U\delta}{\bar{\nu}_1}\frac{\bar{\delta}}{\delta} \sim \frac{\bar{\delta}}{\delta} \gg 1. \tag{A 16}$$

Thus, shock compression and baroclinic torques play a dominant role in the amplification of $\overline{\omega_z'^2}$ across the shock. The viscous diffusion and dissipation effects

are relatively small in the region of the shock wave. The same is true for the enstrophy equation (2.25) presented in § 2. The inviscid mechanisms are modelled in § 3. The viscous dissipation term is later added (§ 4) to capture the turbulence decay on each side of the shock.

REFERENCES

BERNDT, S. B. 1966 The vorticity jump across a flow discontinuity. *J. Fluid Mech.* **26** (3), 433–436.

BOWERSOX, R. D. 2009 Extension of equilibrium turbulent heat flux models to high-speed shear flows. *J. Fluid Mech.* **633**, 61–70.

GUARINI, S. E., MOSER, R. D., SHARIFF, K. & WRAY, A. 2000 Direct numerical simulation of a supersonic turbulent boundary layer at Mach 2.5. *J. Fluid Mech.* **414**, 1–33.

HAYES, W. D. 1957 The vorticity jump across a gasdynamic discontinuity. *J. Fluid Mech.* **3**, 595–600.

HUANG, P. G., COLEMAN, G. N. & BRADSHAW, P. 1995 Compressible turbulent channel flows: DNS results and modelling. *J. Fluid Mech.* **305**, 185–218.

JAMME, S., CAZALBOU, J.-B., TORRES, F. & CHASSAING, P. 2002 Direct numerical simulation of the interaction between a shock wave and various types of isotropic turbulence. *Flow Turbul. Combust.* **68**, 227–268.

KEVLAHAN, N. K.-R. 1997 The vorticity jump across a shock in a non-uniform flow. *J. Fluid Mech.* **341**, 371–384.

KOVASZNAY, L. S. G. 1953 Turbulence in supersonic flow. *J. Aeronaut. Sci.* **20** (10), 657–674.

LARSSON, J. & LELE, S. K. 2009 Direct numerical simulation of canonical shock/turbulence interaction. *Phys. Fluids* **21**, 126101.

LEE, S., LELE, S. K. & MOIN, P. 1993 Direct numerical simulation of isotropic turbulence interacting with a weak shock wave. *J. Fluid Mech.* **251**, 533–562.

MACCORMACK, R. W. & CANDLER, G. V. 1989 The solution of the Navier–Stokes equations using Gauss–Seidel line relaxation. *Comput. Fluids* **17** (1), 135–150.

MAHESH, K., LELE, S. K. & MOIN, P. 1997 The influence of entropy fluctuations on the interation of turbulence with a shock wave. *J. Fluid Mech.* **334**, 353–379.

PASHA, A. A. & SINHA, K. 2008 Shock-unsteadiness model applied to oblique shock-wave/turbulent boundary layer interaction. *Intl J. Comput. Fluid Dyn.* **22** (8), 569–582.

PASHA, A. A. & SINHA, K. 2012 Simulation of hypersonic shock/turbulent boundary-layer interactions using shock-unsteadiness model. *J. Propul. Power* **28** (1), 46–60.

PIROZZOLI, S., GRASSO, F. & GATSKI, T. 2004 Direct numerical simulation and analysis of a spatially evolving supersonic turbulent boundary layer at $M = 2.25$. *Phys. Fluids* **16** (3), 530–545.

ROY, C. J. & BLOTTNER, F. G. 2006 Review and assessment of turbulence models for hypersonic flows. *Prog. Aerosp. Sci.* **42** (7–8), 469–530.

SETTLES, G. S. & DODSON, L. J. 1994 Supersonic and hypersonic shock/boundary layer interaction database. *AIAA J.* **32** (7), 1377–1383.

SINHA, K., MAHESH, K. & CANDLER, G. V. 2003 Modeling shock unsteadiness in shock/turbulence interaction. *Phys. Fluids* **15** (8), 2290–2297.

SINHA, K., MAHESH, K. & CANDLER, G. V. 2005 Modeling the effect of shock unsteadiness in shock/turbulent boundary layer interactions. *AIAA J.* **43** (3), 586–594.

TENNEKES, H. & LUMLEY, J. L. 1972 *A First Course in Turbulence*, p. 66. MIT.

THIVET, F., KNIGHT, D. D., ZHELTOVODOV, A. A. & MAKSIMOV, A. I. 2001 Insights in turbulence modeling for crossing-shock-wave/boundary-layer interactions. *AIAA J.* **39** (6), 985–995.

VEERA, V. K. & SINHA, K. 2009 Modelling the effect of upstream temperature fluctuations on shock/homogeneous turbulence interaction. *Phys. Fluids* **21**, 025101.

WILCOX, D. C. 1998 *Turbulence Modelling for CFD*, 2nd edn. p. 236. DCW Industries.

WILCOX, D. C. 2008 Formulation of the $k - \omega$ turbulence model revisited. *AIAA J.* **46** (11), 2823–2838.